Evaluation of CALIOP 532-nm AOD over Opaque Water Clouds

Zhaoyan Liu[1,2], David Winker[2], Ali Omar[2], Mark Vaughan[2], Jay Kar[1,2], Chip Trepte[2], Yong Hu[2], and Gregory Schuster[2]

[1] {Science Systems and Applications, Inc., Hampton, Virginia}

[2] {NASA Langley Research Center, Hampton, Virginia}

Correspondence to: Zhaoyan.liu@nasa.gov

Abstract

With its height-resolved measurements and near global coverage, the CALIOP lidar onboard the CALIPSO satellite offers a new capability for aerosol retrievals in cloudy skies. Validation of these retrievals is difficult, however, as independent, collocated and co-temporal datasets are generally not available. In this paper, we evaluate CALIOP aerosol products above opaque water clouds by applying multiple retrieval techniques to CALIOP level 1 profile data and comparing the results. This approach allows us to both characterize the accuracy of the CALIOP above-cloud aerosol optical depth (AOD) and develop an error budget that quantifies the relative contributions of different error sources. We focus on two spatial domains: the African dust transport pathway over the tropical North Atlantic and the African smoke transport pathway over the southeastern Atlantic. Six years of CALIOP observations (2007-2012) from the northern hemisphere summer and early fall are analyzed. The analysis is limited to cases where aerosol layers are located above opaque water clouds so that a constrained retrieval technique can be used to directly retrieve 532 nm aerosol optical depth and lidar ratio. For the moderately dense Sahara dust layers detected in the CALIOP data used in this study, the mean/median value of the lidar ratios derived from a constrained opaque water cloud (OWC) technique is 45.1/44.4 ± 8.8 sr, which is somewhat larger than the value of 40 ± 20 sr used in the CALIOP level 2 (L2) data products. Comparisons of CALIOP L2 AOD with the OWC-retrieved AOD reveal that for nighttime conditions the L2 AOD in the dust region is underestimated on average by ~26% (0.184 vs. 0.248). Examination of the error sources indicates that errors in the L2 dust AOD are primarily due to using a lidar ratio that is somewhat too small. The mean/median lidar ratio retrieved for smoke is 69.4/70.4 ± 16.2 sr, which is consistent with the modeled value of 70 ± 28 sr used in the CALIOP L2 retrieval. Smoke AOD is found to be underestimated, on average, by ~39% (0.191 vs. 0.311). The primary cause of AOD differences in the smoke transport region is the tendency of the CALIOP layer detection

scheme to prematurely assign layer base altitudes and thus underestimate the geometric thickness of smoke layers.

1. Introduction

Beginning with the first Intergovernmental Panel on Climate Change (IPCC) assessment, tremendous progress has been made in modeling the global impacts of aerosols on the Earth's climate. Nevertheless, as summarized in the most recent 5th assessment report (Stocker et al., 2013), significant uncertainties remain. Recent model intercomparisons have shown a large diversity in the vertical distribution of aerosols (Kinne et al., 2006; Textor et al., 2006; Huneeus et al., 2011) which can be attributed more to uncertainties in the simulation of aerosol processes than in the realism of the aerosol precursor emissions used by the models. Errors in modeling the vertical distribution of aerosol cause errors in the aerosol atmospheric lifetime and global distribution. In cloudy skies, aerosol radiative forcing can be a strong function of the relative vertical distributions of cloud and aerosol. While comparisons with observations are clearly necessary to evaluate and improve model performance, until recently global measurements of aerosol vertical distribution were notably lacking, largely because previous generations of space-based passive sensors had only limited abilities to retrieve aerosol properties in cloudy skies. (The advent of innovative new retrieval techniques suggests that this situation is now changing for the better; e.g., see Waquet et al., 2009; Torres et al., 2012; Yu et al., 2012; Jethva et al., 2013; and Waquet et al., 2013; and an overview by Yu and Zhang, 2013). However, beginning in June 2006 a global dataset of height-resolved measurements of aerosols and clouds has been continuously acquired by the Cloud-Aerosol Lidar with Orthogonal Polarization (CALIOP), deployed aboard the Cloud Aerosol Lidar and Infrared Pathfinder Satellite Observations (CALIPSO) platform. These active sensor data offer a new and unique opportunity to characterize the global three-dimensional (3D) distribution of aerosol, including aerosol located above low clouds (Winker et al., 2013). Aerosol extinction profiles and aerosol optical depth (AOD) can be derived from the CALIOP measurements even for aerosols located over clouds or other bright surfaces. CALIOP's ability to quantify the spatial distribution and optical properties of above-cloud aerosols represents an important step forward, as this information is required to more accurately assess aerosol intercontinental transport and radiative and climate impacts (Schulz et al., 2006; Chand et al., 2009; Yu et al., 2012).

CALIOP retrievals of AOD in cloud-free skies have been evaluated by comparisons with MODIS-Aqua (Kittaka et al., 2011; Redemann et al., 2012) and with AERONET (Schuster et al., 2012; Omar et al., 2013). Other studies have examined seasonal and regional-mean aerosol vertical distributions for the purpose of model evaluation (Yu et al., 2010; Koffi et al., 2012) and noted deficiencies in the vertical aerosol distributions predicted by the models. Winker et al. (2013) reported an initial evaluation of the accuracy of the CALIOP level 3 (L3, gridded, monthly mean) aerosol extinction profiles. These preliminary results showed that monthly-mean CALIOP aerosol profiles provide quantitative characterization of elevated aerosol layers within major transport pathways, but a more detailed validation of the retrievals of these elevated aerosol layers is needed. Most recently, Kacenelenbogen et al. (2014) evaluated the CALIOP above-cloud aerosol retrieval, by comparing the CALIOP retrieved AOD with the AOD measured by the NASA Langley research Center (LaRC) airborne high-spectral-resolution lidar (HSRL) during 86 coincident flights in North America (mostly in the US and during daytime). Their comparison showed that the CALIOP standard processing can substantially underestimate the occurrence frequency of aerosols when optical depths are smaller than 0.02. This study provides a useful snapshot of CALIOP measurements of tenuous aerosol layers in the free troposphere.

In this paper, we refine a previously developed opaque water cloud (OWC) constrained retrieval technique (Hu et al., 2007) and introduce two variations on the standard CALIOP aerosol extinction retrieval algorithm. We then apply these retrievals to six years of nighttime CALIOP 532 nm Level 1 (L1) profile data in two regions in the Atlantic Ocean to study the optical properties of transported mineral dust and smoke from biomass fires. Finally, these results are used to evaluate the quality of standard CALIOP level 2 (L2) aerosol products and to quantify the contributions from several potential error sources.

2. Spatial Domains Considered

The spatial domains considered in this paper are shown by the red boxes in Figure 1. North Africa is the largest source of dust emissions in the world, injecting large amounts of dust into the atmosphere year round (D. Liu et al., 2008). Transport of Saharan dust across the tropical North Atlantic reaches a maximum during the summer. Cool, moist northeasterly air crossing the Mediterranean into Africa experiences intense heating over the arid continent (e.g., Carlson and Prospero, 1972; Karyampudi et al., 1999). Air over the Sahara is advected westward in the predominantly easterly flow, developing into a dust-laden, well-mixed layer extending from the desert surface to an altitude of several kilometers. As this hot, dry air emerges from the west coast of North Africa, the base of the air mass rises quickly because it is undercut by the relatively cool and moist trade winds. During summer, dust layers are usually confined within the free troposphere by two inversions, one above the dust layer and one below, and are transported westward over several thousand kilometers into the Caribbean and as far as Central America and the Amazon basin. The unique capability of the CALIOP lidar to track this transatlantic transport and to capture the vertical structure of African dust has been documented previously (Liu et al., 2008). For this work we select a region (10°N-30°N, 50°W-15°W) over the North Atlantic where the dust transport is most active and prolific. More importantly, within this region there are extensive stratocumulus decks that lie at the top of the marine boundary layer (MBL) and beneath the dust layers. When these clouds are opaque, the 532 nm cloud integrated attenuated backscatter can be used to derive the optical depth of the overlying aerosol, which can subsequently be used to retrieve an estimate of the dust lidar ratio (i.e., the ratio of extinction to 180°-backscatter, Hu et al., 2007; Liu et al., 2008). Only the most active dust transport months of June – August are considered.

The other region selected is over the southeastern Atlantic off the west coast of southern Africa. Savanna fires are one of the largest sources of black carbon emissions to the atmosphere, with southern Africa being one of the major source regions (Bond et al., 2013). Southern Africa is characterized by intense biomass burning during boreal summer (June to October) (Cooke et al., 1996) and African savannas are the largest single source of biomass burning emissions (Levine et al., 1995). Extensive smoke plumes are advected westward to the southeastern Atlantic. Climate model studies have shown that the climate sensitivity to black carbon can be two or more times larger than that to carbon dioxide for a given top-of-atmosphere radiative forcing (Hansen et al., 1997; Cook and Highwood, 2004). While it is well known that biomass burning aerosols can make a significant contribution to radiative forcing, this contribution is poorly quantified (e.g. Chand et al., 2009). Smoke layers over the southeastern Atlantic generally overlie vast decks of stratocumulus clouds. There is no consensus among models as to even the sign of the direct aerosol forcing in this region (Schulz et al., 2006), in part due to the uncertainty in model-based estimates of the relative vertical locations of the clouds and the transported smoke. Recent studies based on CALIOP observations have investigated the magnitude of the aerosol radiative effect over this region (Chand et al., 2009; Sakaeda et al., 2011). The presence of persistent stratocumulus underneath the smoke layer allows application of the OWC constrained retrieval technique, thus providing an independent retrieval for comparison with the standard CALIOP products. The months considered are from July to September over the six year period (2007-2012).

3. Methodology

In this section we briefly describe the lidar inversion techniques and the algorithms used in CALIOP standard data processing. We also review the opaque water cloud constrained retrieval technique (Hu et al., 2007) which we will use to directly derive the aerosol optical depths above clouds for comparison with the CALIOP standard retrievals. In addition, a rescaling technique applied to the CALIOP L2 data and full-column retrievals that make direct use of the CALIOP L1 data will be used to help further assess the performance of the standard retrieval and to partition contributions of different error sources to the AOD uncertainties.

3.1 Solutions of Lidar Equation

The standard CALIOP data processing retrieves aerosol extinction and backscatter coefficients from the measured profiles via a numerical solution to the lidar equation (Young and Vaughan, 2009). By assuming that the relationship between aerosol extinction and backscatter remains constant within any given layer, the aerosol lidar ratio (i.e., extinction-to-backscatter ratio) is defined by $S_a = \sigma(r)/\beta(r)$, and the solution to the lidar equation can be written as

$$\beta_a(r) = \frac{B'(r)}{\exp\left(-2\eta S_a \int_{r_0}^{r} \beta_a(r')dr'\right)} - \beta_m(r)\,. \qquad (1)$$

In this expression $B'(r) = X(r)/C/\exp\left(-2S_m \int_{r_0}^{r} \sigma_m dr'\right)$ is the lidar return signal, normalized (i.e., recalibrated) at r_0 and corrected for molecular attenuation. $X(r)$ is the range-corrected lidar return signal at range r, C is a calibration coefficient determined at the calibration range r_0, and σ_m is the extinction coefficient due to molecular scattering and ozone absorption. β_a and β_m are the aerosol and molecular backscattering coefficients, respectively, with subscripts a and m representing the aerosol and molecular scattering, respectively. η is the multiple scattering factor (Platt, 1973), and $S_a^* = \eta S_a$ is the effective lidar ratio. The molecular scattering components can be determined using meteorological data from radiosonde measurements or atmospheric models. In the CALIOP data processing, a global meteorological analysis product from NASA's Global Modeling and Assimilation Office (GMAO) is used to calculate the necessary molecular backscatter and extinction coefficients. For version 3 (V3) CALIOP lidar retrievals, the data calibration at 532 nm is performed by comparing return signals from 30 – 34 km altitudes with a molecular reference profile (Powell et al., 2009). Assuming that S_a and η can be specified *a priori*, the remaining unknown quantity in Eq. (1) is $\beta_a(r)$, which is present on both sides of the equation, thus necessitating an iterative numerical solution.

The aerosol lidar ratio, S_a, is a key parameter in the lidar inversion. S_a is an intrinsic optical property of aerosols that varies depending on the aerosol composition, size distribution, and shape. Once S_a is determined, both the aerosol backscatter coefficient, β_a, and extinction, σ_a, can be retrieved. The retrieval accuracy is often dominated by uncertainties in S_a (Young et al., 2013).

3.2 CALIOP Data and Standard Level 2 Retrieval

CALIOP transmits linearly polarized laser light at 532nm and 1064 nm. The CALIOP receiver resolves the polarization state of the 532 nm backscatter signals by separately measuring light polarized parallel and perpendicular to the polarization plane of the outgoing 532 nm beam. Backscatter signals are sampled at a vertical resolution of 30 m below an altitude of 8.2 km and at 60m between 8.2 km and 20.2 km. The primary CALIOP L1 data products are calibrated attenuated backscatter profiles measured for each laser shot corresponding to a horizontal resolution of 333 m. Because of the presence of some amount of stratospheric aerosols in the V3 calibration region (30-34 km), the V3 L1 profiles can be biased low by a few percent (Rogers et al., 2011). To correct this, all the V3 L1 profiles were recalibrated in this paper using calibration coefficients determined at altitudes of 34-40 km (Vernier et al. 2009).

After calibration and range registration, atmospheric layers are detected using a threshold technique applied to profiles of 532 nm attenuated scattering ratio (Vaughan et al., 2009). Dense clouds can be detected in single-shot profiles, while detection of aerosol layers usually requires averaging of multiple lidar shots. A nested, multi-grid averaging scheme is employed to maximize layer detection probabilities across the broadest possible range of backscatter intensities. To avoid cloud contamination of the aerosol data, boundary layer clouds detected at single shot resolution are identified and removed before further horizontal averaging and subsequent searches for more tenuous layers (Vaughan et al., 2009). After layer detection, a cloud-aerosol discrimination (CAD) algorithm is applied to separate clouds and aerosols (Liu et al., 2009). This CAD process is followed by an algorithm which determines the aerosol type. Six aerosol types have been defined for the CALIOP retrieval (Dust, Polluted Dust, Marine, Clean Continental, Pollution, and Smoke or Biomass Burning). Each aerosol type is characterized by a mean lidar ratio that varies from 20-70 sr (Omar et al., 2009). Aerosol extinction is then retrieved at 532 nm and 1064 nm, using lidar ratios selected according to the aerosol typing results (Young and Vaughan, 2009). Aerosol extinction retrievals are only performed within detected layers, as the CALIOP signal-to-noise ratio (SNR) does not permit high quality retrievals in clear air at the spatial resolution of the L2 products.

Three steps are involved in producing the CALIOP standard L2 data products (Winker et al., 2009). First, cloud and aerosol layers are identified by a set of algorithms, referred to as the selective iterative boundary locator (SIBYL; Vaughan et al., 2009), which are applied to the 532 nm attenuated backscatter profiles. Second, using data from all three CALIOP channels (532 nm parallel and perpendicular channels and 1064 nm channel), layers are identified as clouds or aerosols (Liu et al., 2009) and the aerosol type (Omar et al., 2009) and cloud ice-water phase (Hu et al., 2009) are determined. Finally, profiles of particle backscatter and extinction coefficients are retrieved by the hybrid extinction retrieval algorithm (HERA; Young and Vaughan, 2009). HERA performs retrievals only within the layer boundaries identified by SIBYL using the iterative numerical approach (i.e., Eq. (1)) and the inversion is initiated at the top of the layer. The retrieval requires knowledge of the layer multiple scattering factor, η, and layer lidar ratio, S_a. In the V3 aerosol retrieval, $\eta = 1$ for all aerosol species. Because of this treatment for the multiple scattering, the extinction coefficients and AODs reported in the V3 data products should be considered as effective values, with the multiple scattering contributions that depend to some extent on both the aerosol loading and the aerosol optical and microphysical properties. However, our simulations (Winker, 2003; Liu et al., 2011) have shown that multiple scattering is a small effect within moderately dense dust layers and insignificant for smoke (also see Figure 9 in subsection 4.2 that supports the idea that multiple scattering effects in moderate dust are small). η for dust may be reduced somewhat in the next data release, based on these previous results. Based on comparisons to field measurements and simulations using large particle sizes measured in the source regions, Wandinger et al. (2010) assert that a more significant multiple scattering correction is needed for the CALIOP dust measurements, and that failing to make this correction can cause underestimates of 10–40% in the extinction retrievals. Further work is planned in this area.

S_a is generally selected based on the results of the aerosol typing, though it can be derived directly on rare occasions when the air above and below an aerosol layer is free of particles (e.g., as in Young, 1995). Aerosol layers are detected iteratively by SIBYL at horizontal resolutions of 5 km, 20 km, and 80 km and the L2 retrieval is performed for all aerosol layers detected at each of these resolutions. Extinction and backscatter profiles are populated in the CALIOP L2 aerosol profile products at a 5-km horizontal resolution. For the layers detected at 20 km or 80 km, the retrieved extinction and backscatter coefficients are replicated over, respectively, 4 or 16 consecutive 5-km profile segments.

3.3 Rescaling Level 2 AOD

In addition to noise, which is the primary source of random error in the CALIOP measurements and the corresponding L2 data products, there are also other sources of error in the derivation of AOD. These include failure to detect the full extent of aerosol layers, due either to SNR-imposed detection limits or algorithm deficiencies, misclassification during aerosol typing, and/or the use of an inaccurate lidar ratio. We cannot simply estimate the AOD error as proportional to the lidar ratio error because the relationship is nonlinear (Winker et al. 2009). Instead, to evaluate the impact of lidar ratio errors on AOD due to misclassification of aerosol type, we calculate a rescaled AOD using a procedure similar to the method described in Lopes et al. (2013).

(a) Integrate the above-cloud aerosol extinction profile to obtain an above-cloud column AOD estimate, τ_{above}, based on the L2 aerosol type and lidar ratio assignments.

(b) Use τ_{above}, the S_{a} assigned by the CALIOP aerosol subtyping algorithm, and an assumed multiple scattering factor of $\eta = 1$ to derive an estimate of the layer integrated attenuated backscatter via Platt's equation (Platt, 1973):

$$\gamma'_{eff} = \int_{r_{top}}^{r_{base}} \beta_a(r) T_a^2(0,r)\, dr = \frac{1-\exp\left(-2\eta\,\tau_{above}\right)}{2\eta S_a} \tag{2}$$

where $T_a^2(0,r) = \exp\left(-2\int_0^r \sigma_a(r')\,dr'\right)$ is the aerosol two-way transmittance between the lidar and the aerosol layer base. For cases where multiple aerosol layers are detected and classified as different aerosol types in the column above an opaque water cloud, Eq.(2) becomes $\gamma'_{eff} = \sum_{i_{type}} \frac{1-\exp\left(-2\eta\,\tau_{above}(i_{type})\right)}{2\eta S_a(i_{type})}$, where i_{type} represents the layer aerosol type, and $S_{\mathrm{a}}(i_{\mathrm{type}})$ and $\tau_{\mathrm{above}}(i_{\mathrm{type}})$ are, respectively, the lidar ratio and the optical depth retrieved for the aerosol of type i_{type}.

(c) Using γ'_{eff} and the lidar ratio for the appropriate aerosol type (dust or smoke), derive an estimate of the rescaled AOD using

$$AOD_{rescaled} = -\frac{1}{2\eta S_{a,model}} \ln\left(1 - 2\eta S_{a,model}\, \gamma'_{eff}\right) \tag{3}$$

where once again $\eta = 1$ and $S_{\mathrm{a,model}}$ is either 40 sr (dust) or 70 sr (smoke). Like the L2 AOD, the rescaled AOD is an effective one because η is assumed to be 1.

This procedure is applied in the dust and smoke transport regions, assuming that only dust or smoke is the dominant aerosol type in the respective region. While there are always maritime aerosols in the MBL in both regions, for the aerosol above cloud cases considered in this paper, boundary layer clouds effectively separate the transported aerosol layers in the free troposphere from the MBL. It is thus highly likely that the above-cloud layers are either dust or smoke, depending on region, and are not mixed with marine aerosol. Further, during the summer months considered in this paper, there is a little chance that cross transport occurs between the two regions, which would presumably produce something akin to the CALIOP polluted dust model. Dust transport and biomass burning activities show a strong seasonal dependence in Africa. In summer, the transport of dust generated in the North Africa occurs primarily over the North Atlantic (D. Liu et al., 2008), while the biomass burning is only active in southern Africa (Haywood et al., 2008). Furthermore, while southern Africa has a large area of arid terrain, it is not a major source of dust production (Washington et al., 2003). A study based on the first year of the CALIOP measurements (D. Liu et al., 2008) revealed that the occurrence frequency of airborne dust over the southern Africa was small (only few percent for some locations), suggesting that the dust from sources in southern Africa is not readily mobilized by the typical meteorology of the area (Washington et al., 2003). Therefore, the occurrence of dust mixed with smoke (i.e., “polluted dust”) is expected to be small in both regions examined in this study.

3.4 Opaque Water Cloud Constrained Retrieval

When the layer optical depth is available as a constraint, β_a, σ_a and S_a (or the effective lidar ratio, $S_a^* = \eta S_a$, when multiple scattering effects must be considered) can all be retrieved directly. One well-developed technique to determine the layer optical depth uses the molecular scattering above and below the layer to derive the required constraint (Sassen and Cho, 1992; Young, 1995). When the molecular scattering can be measured in clean air on both sides of a layer, the transmittance (and hence the optical depth) of the layer can be derived by comparing the return signals above and below the layer to a molecular scattering profile derived from rawinsonde measurements or meteorological model data. This technique is applied to the CALIPSO measurements at 532 nm for transparent cirrus clouds in the upper troposphere where the air is generally clean on both above and below the clouds (Young and Vaughan, 2009). Aerosol layers are, however, generally located in the lower troposphere and such clean regions are seldom available.

Hu et al. (2007) developed a technique for the CALIOP measurements that uses opaque water clouds as a reference to determine the optical depth of overlying transparent aerosol or cirrus layers (e.g., as in Fig. 4). This approach takes advantage of the relatively small variation of water cloud lidar ratios (e.g., Pinnick et al., 1983; O’Connor et al., 2004; Hu et al., 2006), and the well-behaved relationship between the layer-integrated depolarization ratio and the multiple scattering in the layer-integrated attenuated backscatter from water clouds, as described in Hu (2007) by

$$\mathrm{H} = \frac{\gamma'_{WC,SS}}{\gamma'_{WC,MS}} = \left(\frac{1-\delta_I}{1+\delta_I}\right)^2 \tag{4}$$

where H is the layer effective multiple scattering factor and δ_I is the layer-integrated volume depolarization ratio, and the subscripts WC, SS and MS represent, respectively, water clouds, single scattering and multiple scattering. The multiple scattering factor that is considered constant in Eq. (1) originally defined in terms of the ratio of single-scattered and multiply-scattered signals from range r, such that $\eta(r) = 1 - \ln\left[B'_{MS}(r)/B'_{SS}(r)\right]/2\tau(r)$ (Platt, 1973). On the other hand, it is more straightforward define H as the ratio of the integrated attenuated backscatter from single scattering only $\left(\gamma'_{WC,SS}\right)$ to the total integrated attenuated backscatter, which includes contributions from multiple scattering $\left(\gamma'_{WC,MS}\right)$. $\gamma'_{WC,MS} = \int_{r_{WC,top}}^{r_{WC,base}} B'(r)dr$ is the layer-integrated attenuated backscatter calculated from opaque water clouds measured by CALIOP (Vaughan et al., 2009), and thus includes not only multiple-scattering effects but also additional attenuation from any overlying cloud or aerosol layers (Hu et al., 2007). The layer-integrated attenuated single-scattering backscatter for a cloud with no aerosol (NA) located above can be calculated using Platt's equation:

$$\begin{aligned} \gamma'_{WC,SS,NA} &= \int_{r_{WC,top}}^{r_{WC,base}} B'_{SS}(r)dr = \frac{1-\exp(-2\tau)}{2S_{WC}}; \\ &\approx \frac{1}{2S_{WC}}, \quad \text{for opaque water clouds } (\tau > \sim 3), \end{aligned} \tag{5}$$

The last expression holds for water clouds with optical depths greater than about 3. S_{WC} is the water cloud lidar ratio and τ is the cloud optical depth. From Mie calculations based on in-situ measurements of water cloud size distributions (Hu et al., 2006; also see Fig. 2), S_{WC} is found to vary insignificantly for a variety of water clouds, having a mean value of 18.9 sr and a standard deviation of 0.25 sr over ocean and 0.47 sr over land. The presence of a semi-transparent aerosol layer above an OWC will reduce $\gamma'_{WC,SS,NA}$ by an amount equal to the two-way transmittance, $\exp(-2\tau_{aerosol})$, of the aerosol layer; i.e., $\gamma'_{WC,SS} = \exp(-2\tau_{aerosol})\gamma'_{WC,SS,NA}$, where $\tau_{aerosol}$ is the optical depth of overlying aerosol layer (Hu et al., 2007). Therefore,

$$\tau_{aerosol} = -\frac{1}{2}\ln\left(\frac{\gamma'_{WC,SS}}{\gamma'_{WC,SS,NA}}\right), \tag{6a}$$

$$= -\frac{1}{2}\ln\left(\frac{\mathrm{H}\gamma'_{WC,SS}}{\frac{1}{2S_{WC}}}\right) = -\frac{1}{2}\ln\left(2S_{WC}\gamma'_{WC,MS}\left(\frac{1-\delta_I}{1+\delta_I}\right)^2\right). \tag{6b}$$

The layer-integrated depolarization ratio within the cloud layer, δ_I, is calculated from the perpendicular and parallel components of attenuated backscatter measured at 532 nm, $\beta'_\perp$ and $\beta'_\parallel$,

$$\delta_I = \frac{\int_{r_{WC,top}}^{r_{WC,base}} B'_\perp(r)dr}{\int_{r_{WC,top}}^{r_{WC,base}} B'_\parallel(r)dr}. \tag{7}$$

The AOD determined using the OWC technique can be used as a constraint to retrieve backscatter and extinction profiles and lidar ratio of the overlying aerosol layer. For the cases selected and analyzed in this paper, the underlying clouds are opaque boundary layer clouds with cloud-tops lower than 2 km. Given the relatively small footprint of the CALIOP lidar (100 m), for single-shot retrievals, it is not necessary that the clouds be overcast on any significant horizontal scale, and the retrieval appears to work even in broken stratocumulus. A closer examination shows that the temperatures at the top of these opaque clouds typically range from 8°C to 25°C, confirming that these clouds are water.

Retrievals from measurements made by passive satellite sensors such as MODIS (Zhang and Platnick, 2011) produce effective radii for water clouds that are generally larger than those obtained from in-situ measurements (Miles et al., 2000). To represent these larger droplet sizes we have extended the previously reported Mie calculations to cloud particle sizes larger than 15 μm. The results are presented in Fig. 2 (solid green squares). For these larger effective radii, the water cloud lidar ratio shows a significant dependence on droplet size. Furthermore, the possibility of encountering these large droplet sizes precludes the use of a theoretical calculation of $\gamma'_{\mathrm{WC,SS,NA}}$ and highlights the need to use an empirically derived, location-dependent S_{WC} in the OWC AOD retrieval.

We examined $\gamma'_{WC,SS,NA}$ and $S_{WC} = 1/2\gamma'_{WC,SS,NA}$ for opaque water clouds based on the CALIOP measurements made during June – September from years 2007 – 2012. $\gamma'_{WC,SS,NA}$ is calculated using

$\gamma'_{WC,SS,NA} = \gamma'_{WC,MS,NA}\mathrm{H}$, where $\gamma'_{WC,MS,NA} = \int_{r_{WC,top}}^{r_{WC,base}} B'(r)dr$ is the integrated attenuated backscatter of an opaque water cloud layer, r_{base} and r_{top} are respective the apparent base and top of the cloud, and H is calculated using Eq. (4) from the layer-integrated depolarization ratio δ_l of the cloud as defined in Eq.(7). Regional maps of $\gamma'_{WC,SS,NA}$ and S_{WC} are presented in Fig. 3. Results shown are based on profiles where no aerosols or clouds were detected by the feature finding algorithms above those opaque water clouds with tops below 2 km. To further ensure aerosol-free conditions above cloud top, the layer-integrated attenuated scattering ratio (ASR), $\int_{r_{WC,top}}^{8km} B'dr / \int_{r_{WC,top}}^{8km} \beta_m dr - 1$, was required to lie between -0.05 and 0.05. Figure 3 also shows the spatial dependence of the retrieved values of $\gamma'_{WC,MS,NA}$ (3c), H (3d), $\gamma'_{WC,SS,NA}$ (3e) and S_{WC} (3f), with most OWCs being found over the oceans (panels (3a) and (3b)). S_{WC} is generally larger (i.e., smaller droplet sizes, refer to Fig. 2) over the downwind coastal regions or along the aerosol transport pathways and smaller (larger cloud droplet sizes) in the South Atlantic than in the North Atlantic. This spatial distribution pattern is generally as what people expect for the distribution of low cloud droplet sizes. The largest difference between theoretical expectations and the empirically derived values of $\gamma'_{WC,SS,NA}$ is a northeastward decreasing trend from ~0.03 to ~0.023 sr^{-1}s seen in the smoke transport region. Given this variability, the use of a constant $\gamma'_{WC,SS,NA}$ or S_{WC} could introduce errors as large as ~0.1 in the retrieved AOD. For this reason, Eq. (6a) and a regionally varying $\gamma'_{WC,SS,NA}$ are used to derive AOD in this paper. On the other hand, $\gamma'_{WC,MS,NA}$ shows a different spatial distribution pattern. It is generally larger over the eastern Atlantic close to the African continent. This may indicate a larger number concentration of the cloud droplets. $\gamma'_{WC,MS,NA}$ includes contributions from multiple scattering and multiple scattering generally increases as the number concentration of water droplets increases.

Figure 4 shows an example of (a) the CALIOP measured attenuated backscatter and (b) the ratio of attenuated backscatter (or color ratio) at 1064 nm and 532 nm, along with (c) the L2 vertical feature mask (VFM) and (d) the results of the aerosol subtyping algorithm. These observations are from a nighttime orbit passing over the western coast of Africa on August 19, 2013. Dust and smoke aerosols and high and low clouds were all observed in this scene. Shown in Fig. 5 are profiles of attenuated backscatter at (a) 532 nm and (b) 1064 nm averaged over 20 km around 10°S in Fig. 2. The corresponding molecular scattering profiles are indicated by dashed lines. The brown and blue segments in Fig. 5a show a smoke aerosol layer (brown) and an opaque water cloud layer (blue) as detected by the standard CALIOP L2 layer detection algorithm, which is applied to the 532 nm data only. However, in the 1064 nm profile shown in Fig. 5b, the base of the smoke layer is seen to extend down to the top of the water cloud. Below about 2.5 km, the 532 nm signal levels of this layer fall below the detection threshold, and thus the lower part is not successfully detected by the standard data processing. The 1064 nm signal routinely penetrates further into smoke layers because the extinction of smoke aerosols is typically 2-3 times smaller at 1064 nm than at 532 nm. However, the standard L2 extinction retrieval is only applied in those regions where a layer was detected in the 532 nm profile; i.e., in this example between ~4.5 km and ~2.5 km. Since this same 'retrieve in detected layers only' restriction is applied at both wavelengths, and since V3 layer detection is only done at 532 nm, extinction coefficients at 1064 nm are likewise only retrieved between ~4.5 km and ~2.5 km. The averaged 532 nm aerosol extinction profile from the L2 profile products (brown) is shown in Fig. 5c.

The OWC constrained retrieval is initiated at a fixed altitude of 8 km and continues downward to an altitude ~0.2 km above the apparent cloud top determined by the L2 processing. The OWC constrained retrieval is performed iteratively, using a set of trial values of lidar ratio to generate extinction profiles via Eq. 1. A lidar ratio solution is determined as the value that produces the best match between the integrated extinction profile retrieved from above the water cloud and the OWC AOD. An extinction profile retrieved using the OWC AOD as a constraint is also presented in Fig. 5c (light green). The OWC-constrained retrieval successfully captures the lower part of the smoke layer that is missed in the L2 processing. Above the smoke layer (~4.2 km) the retrieved extinction varies largely due to noise and at a level comparable to the calibration error. After the aerosol extinction is retrieved, particulate depolarization ratio (PDR), another aerosol intrinsic property, can be retrieved from the two measured polarization components of backscattered signals at 532 nm using

$$\delta_a(r) = \frac{B'_{\perp}(r)\exp\left(2\int_{r_{top}}^{r}\sigma_a(r)dr\right) - \beta_m(r)\frac{\delta_m}{1+\delta_m}}{B'_{\parallel}(r)\exp\left(2\int_{r_{top}}^{r}\sigma_a(r)dr\right) - \beta_m(r)\frac{1}{1+\delta_m}} \tag{7}$$

where δ_m is the molecular depolarization ratio, with a value of ~0.0036 for the spectral bandwidth of the CALIOP receiver (Powell et al., 2009).

In this paper, retrievals using the OWC technique are performed on CALIOP V3 L1 attenuated backscatter profiles, averaged horizontally to 5 km. Fifteen recalibrated L1 profiles are averaged to create each 5-km profile. V3 VFM products are used to identify feature locations and find OWCs. The OWCs selected for constrained retrievals are (1) single layered with (2) top heights less than 2 km for which (3) opaque water clouds are detected in all 15 single-shot profiles within each 5-km average, and the standard deviation of these 15 single shot top heights is less than 50 m. Criterion #3 ensures that the cloud tops were relatively uniform throughout the 5-km horizontal extent. The selected OWCs are then sorted into two subsets: those with aerosols located above the clouds and those without (based on the VFM and with |ASR| < 0.05). Imposing a criterion of |ASR| < 0.05 ensures that the AOD above the clouds is less than ~0.02, even for strongly absorbing aerosols such as smoke. The subset of OWCs with no overlying aerosols in a 2°×3° (lat×lon) grid box was used to calculate a reference which is used in Eq. (6a) to retrieve AOD from the subset with overlying aerosol. The results shown in Fig. 3 are based on the subset of the opaque water clouds without overlying aerosols.

3.5 Full Column Retrieval

The CALIOP feature detection algorithm sometimes cannot successfully detect weakly scattering parts of an aerosol layer or lower parts of highly attenuating aerosol layers, as discussed earlier (also see Figs. 4 and 5). This causes the retrieved AOD to be biased low. To help evaluate the impact of potential failures in detecting full extent of aerosol layers, we also performed full column (FC) retrievals, where the retrieval is initiated at a fixed altitude of 8 km and proceeds downward using a fixed lidar ratio. We use a set of fixed lidar ratios incremented by 5 sr (i.e., 40, 45, etc…) plus the modeled values used in the CALIOP L2 retrievals for different aerosol types. The FC retrieval differs from the CALIOP standard L2 retrieval in that the L2 extinction retrieval is only applied between the apparent top and base of the aerosol layers detected by the SIBYL layer detection algorithm, whereas the FC retrieval is applied to the full vertical column extending from 8 km down to 0.2 km above the L2-identified top of the underlying OWC, in hopes recapturing some of the aerosols that may have been missed by the feature detection algorithm. The FC retrieval is terminated at 0.2 km above the apparent top of the underlying OWC to avoid possible contamination of cloud edges in the aerosol retrieval. The starting altitude of 8 km was chosen because the transported aerosol in the two selected spatial domains appears to be lower than this altitude. For example, consider the smoke layer around 6.61°S in Fig. 4. Because of the large attenuation at 532 nm (Fig. 5a), the attenuated backscatter coefficients in the lower part of the layer fall below the SIBYL detection threshold, and thus SIBYL detects the base of this layer at ~3 km (Fig. 5c). However, as seen in Fig. 5b, the true aerosol layer base appears to extend to the top of the underlying cloud at ~1.5 km. For this example, the L2 retrieval would only apply to the upper part of this layer between ~5 km and ~3 km and hence miss the lower part of this layer between ~3 km and ~1.5 km and therefore underestimate AOD of the layer (e.g., see Kim et al., 2013, Torres et al., 2013). Because the FC algorithm performs the retrieval from 8 km down to the cloud top at ~1.5 km, the optical depths retrieved by the FC method provide a useful reference to diagnose and evaluate failures to detect the full extent of aerosol layers in the standard retrieval.

4. Results

Six years (2007 – 2012) of CALIOP data from the two regions indicated in Fig. 1 have been analyzed using the OWC constrained technique. The analyses were restricted to nighttime measurements, as the large amount of solar background noise present in daytime measurements require signal averaging over longer distances (e.g., 20 km), which would require opaque clouds with corresponding larger horizontal extents and hence significantly reduce the total number of samples available. Results are presented and discussed in the following subsections.

4.1 Spatial Distributions from OWC Retrievals

Because accurate knowledge of $\gamma'_{WC,SS,NA}$ is so important in the derivation of AOD using the OWC technique, in this subsection we examine the spatial variability of $\gamma'_{WC,SS,NA}$ and its potential impact on the retrieved AODs. To obtain more insight we look into the spatial distributions of dust and smoke optical properties retrieved using the OWC technique. Figures 6 and 7 present 2°×3° resolution maps of (a) the number of samples acquired, (b) mean AOD_{OWC}, (c) mean S_a and (d) PDR of aerosol layers using the OWC constrained retrieval technique, respectively, for the dust and smoke transport regions. AOD_{OWC} was calculated using Eq. (6a) with a location-dependent

$\gamma'_{WC,SS,NA}$. Panels (e) through (h) in Figs. 6 and 7 show the same quantities for the data screened using ASR>0.3 for the dust region and ASR>0.2 for the smoke regions. The ASR threshold for the smoke region is smaller than for the dust region because for the same extinction the backscatter at 532 nm is smaller for smoke than dust due to the difference in the lidar ratios. Panels (j) through (l) in each figure are the corresponding properties retrieved using a constant value of $\gamma'_{WC,SS,NA}$ which was averaged over the entire red box for each selected spatial domain, and panels (n) through (p) are the differences between these retrieved properties using a location dependent $\gamma'_{WC,SS,NA}$ (as in panels (j) through (l)) and a constant $\gamma'_{WC,SS,NA}$ (as in panels (f) through (h)).

Most OWCs are observed just offshore over the northeastern Atlantic and southeastern Atlantic, in the trade wind regions. As expected, $\mathrm{AOD_{OWC}}$ is the largest in the coastal regions near the sources in the northern and southern Africa and decreases gradually as dust or smoke is transported farther from the sources.

The S_a retrieval is sensitive to errors and biases in the $\mathrm{AOD_{OWC}}$ and to the noise in the above-cloud backscatter signals. This is especially noticeable when the overlying aerosol layers are optically thin, as will be discussed further in the following subsections. Partly due to this, we see large variations in the retrieved S_a at the edges of the dust transport pathway (Fig. 6c) where $\mathrm{AOD_{OWC}}$ is small (Fig. 6b). We also see that the retrieved S_a values are larger outside of the typical dust transport pathway, where the occurrence of dust is less frequent. The PDR, retrieved using Eq. (7) and shown in Fig. 6d, generally has smaller values north of ~30°N and south of ~10°N, which suggests that relatively large amounts of other aerosol types are present outside of the dust transport pathway. North of ~30°N the westerly wind (Fig. 1) can carry anthropogenic aerosols having large S_a values from North America to the northwest coast of Africa. South of ~10°N, the southeasterly trade wind can bring biomass burning aerosol from central Africa to the tropical North Atlantic (Fig. 1). At 532 nm, biomass burning aerosols (smoke) generally have S_a values larger than dust, as seen by comparing Figs. 7c and 7g to Figs. 6c and 6g. The retrieved S_a and PDR for dust are distributed more uniformly when weakly scattering aerosol layers are screened out using ASR>0.3. This is as generally expected and instills confidence in our analysis results. Since a sizeable fraction of North Africa is covered by deserts, desert dust is a dominant aerosol type in this region all year long. During summer, the transport of dust over the Atlantic is usually confined to the free troposphere by two inversions and hence the dust size distribution can remain largely unchanged during the course of transport across the Atlantic Ocean (Maring et al, 2003). More uniform distributions of mean S_a and PDR are expected where dust is dominant. Large values (> 60 sr) are, however, still seen south of 10°N, where the transported biomass burning aerosol is relatively dense and dominant. We note that while the mean S_a shown in Fig. 6 has a relatively uniform spatial distribution, the individual values of S_a averaged in each grid box vary considerably. As will be discussed in the next subsection (see Fig. 8), this variability in S_a may reflect an underlying variability in the origin of different dust plumes. The relatively uniform distribution of the mean S_a may simply indicate that, within each grid box, the probabilities of dust transport originating from different source regions are similar.

When a constant $\gamma'_{WC,SS,NA}$ (or S_{WC}) is used, as in the previous work of Chand et al., 2009 and Sakaeda et al. 2011, a larger spatial trend is seen both in the S_a (Fig. 6k) and the PDR (Fig. 6l) retrieved for dust. A more significant trend is also seen in the retrieved S_a for smoke (Fig. 7k). The large spatial trend in the retrieved S_a when using a constant $\gamma'_{WC,SS,NA}$ does not appear to be realistic and is correlated with the $\gamma'_{WC,SS,NA}$ distribution in Fig. 3, indicating that the large trend in the aerosol retrievals is actually an artifact introduced by the use of a constant $\gamma'_{WC,SS,NA}$. The use of a constant $\gamma'_{WC,SS,NA}$ can overestimate smoke AOD by ~0.1 near the source and S_a by ~10 sr in the northern part of the selected smoke region, while at the same time underestimating these properties in the southwestern part of the region.

4.2 Dust Intrinsic Optical Properties

One-dimensional (1D) and two-dimensional (2D) histograms of the retrieved S_a and PDR using a location-dependent $\gamma'_{WC,SS,NA}$ within the spatial domain as defined by the red box over the dust transport region are presented in Figs. 8a through 8d. The distributions of the retrieved S_a and PDR (Figs. 8c and 8d) are somewhat asymmetric. The mean value of the dust lidar ratio distribution is 50.5 sr, with a median of 45.5 sr, a mode of 44.0 sr, and a standard deviation of 26.4 sr, while for the PDR distribution the mean is 0.222, the median is 0.277, the mode is 0.280, and the standard deviation is 4.24 (this large value is due to a few outliers that have huge values). When weakly scattering layers are screened out using ASR>0.3, the S_a and PDR distributions become more symmetric. The mean, median, mode and standard deviation of the screened S_a data are, respectively, 45.1, 44.4, 43.3 and 8.8 sr, and, respectively, 0.281, 0.281, 0.283 and 0.044 for the screened PDR data. For either the screened or the unscreened data, the modeled S_a value (40 sr) used to produce CALIOP V3 data is ~10% smaller than the OWC retrieved value (Fig. 8c).

The dust S_a values reported in this work fall well within the range of the natural variability of dust lidar ratios previously reported in the scientific literature. An earlier case study based on CALIOP measurements (Liu et al., 2008) tracked a dust event that occurred on August 17, 2006 in North Africa and was subsequently transported across the Atlantic Ocean over the course of several days. The retrieved S_a at 532 nm for this event was 41 ± 3, 41 ± 4, 41 ± 6 sr, respectively, at locations near the source, over the eastern and central Atlantic Ocean. The dust was moderately dense with its AOD at 532 nm decreasing from 0.6 – 1.2 near the source to 0.29 far from the source. The NASA LaRC's airborne HSRL (Hair et al, 2008) measured a lidar ratio of 45.8 ± 0.8 sr and AOD of 0.08 – 0.09 for the dust transported into the Gulf of Mexico 10 days later. Another study (Liu et al., 2011) using multiple years of the CALIOP measurements derived a S_a distribution for opaque dust layers (AOD> ~2) over North Africa with a mean value of 38.5±9.2 sr. It was shown that multiple scattering in these opaque dust layers can decrease the effective lidar ratio by 10% or more relative to the semi-transparent layers analyzed here with the OWC technique.

Shipborne Raman lidar measurements in May 2013 tracked the Saharan air layer across the tropical Atlantic (Kanitz et al., 2014). A 532 nm S_a of 45 sr was measured for aged dust that was ~4500 km away from the North Africa, and 50 sr for dust ~800 km off the coast of the North Africa. The layers observed ~800 km off the coast were not pure dust, but instead were dust mixed with smoke which generally has higher S_a values than dust. Over dust source regions in Morocco, S_a was observed in a range of 38-50 sr by an airborne HSRL for pure dust over Morocco during the SAMUM 2006 campaign (Esselborn et al., 2009). Meantime, a range of 53-55±7 sr was observed for selected dust events by ground-based Raman lidars operated at the airport of Ouarzazate in Morocco (Tesche et al., 2009). Back trajectory analyses show that the observed variability in lidar ratio is primarily attributable to differences in source regions. The large deviation of S_a retrieved in this study (Figs. 8a and 8c) may partly reflect the dependence of the dust optical properties on the sources. Computations based on in-situ measurements (Omar et al., 2010) and AERONET retrievals (Cattrall et al., 2005; Schuster et al., 2012) also produce dust S_a values that vary from ~40 sr to ~55 sr depending on the observation sites. In the remote transport sites in the Gulf of

Mexico and Caribbean Sea, S_a values measured by the LaRC HSRL for an apparently pure dust (depolarization ratio of 0.31-0.33) transported from the North Africa range from 45 to 51 sr (Burton et al., 2013).

PDR is another intrinsic optical property of aerosols. Dust generally has relatively large PDRs due to the irregular shapes and large sizes of dust particles compared with other types of aerosol. Pure dust can have a PDR larger than 0.3. As with the lidar ratios, the dust PDRs reported in this work are consistent with previously reported values. The PDR obtained in the CALIOP case study mentioned earlier (Liu et al., 2008) is ~0.32, and this remained nearly unchanged during the course of the dust transport from the source into the Gulf of Mexico. For a four month dataset of CALIPSO measurements, the PDR retrieved for all single dust layers with optical depths greater than 0.1 over the North Africa has a mean value of 0.3±0.07 (Liu et al, 2011). The PDR value measured at 532 nm for pure dust layers during the SAMUM 2006 campaign is 0.31±0.03 (Freudenthaler et al., 2009; Esselborn et al., 2009). In the Caribbean Sea, the transported pure Sahara dust has PDRs ranging from 0.30 to 0.35 (Burton et al., 2013). The retrieved PDR for the relatively dense aerosol layers (ASR>0.3) over the North Atlantic reported in this paper has a median value of 0.281 ± 0.044, indicating that these aerosol layers are dominated by dust particles. For the weakly scattering layers (refer to Fig. 6), the retrieved S_a tends to be larger and PDR tends to be smaller, implying that the relative concentration of dust particles is smaller compared with the optically thick cases. These optically thin layers are most likely mixtures of dust and continental pollution or biomass burning smoke.

For comparison we present in Fig. 9b the measurements made by the LaRC HSRL during nine CALIOP validation flights during August 11-28, 2010 over the Caribbean Sea. Based on the classification scheme by Burton et al. (2012), four major modes are seen - dust (North Africa origin), marine, a mixture of dust and marine, and urban/smoke. In addition, there is a transitional leg between the Urban/smoke mode and the marine + dust mode which can be a mixture of these two types of aerosol. Shown in Fig. 9a is a composite distribution made from the OWC constrained retrieval for the spatial domain along the Saharan dust transport pathway over the North Atlantic (i.e., Fig. 8b) and for the spatial domain along the smoke transport pathway over the South Atlantic (i.e., Fig. 10b). The OWC retrieved distribution is seen to compare very well with the HSRL measured distribution for dust, although the PDR measured by CALIOP is noisier than that by

HSRL. The mode values for the dust S_a and PDR measured by HSRL are ~44.5 sr and ~0.315, respectively.

4.3 Smoke Intrinsic Optical Properties

Figure 10 shows results from the spatial domain indicated by the red box in Fig. 7. The S_a values retrieved using AOD_{OWC} as a constraint have mean/median/mode values of 74.8/ 71.8/69.8±26.5 sr for all the data and 70.8/70.4/69.6±16.2 sr for screened data. The S_a distribution in the smoke region (Fig. 7g) is not as uniform as in the dust region (Fig. 6g) even after screening out weakly scattering layers. Unlike North Africa, where the landmass is largely desert and desert dust is a dominant aerosol type, in central and southern Africa, the human population density is higher and the surface type is more variable. While smoke is the dominant aerosol type during the austral winter, when biomass burning is active, several other types of anthropogenic aerosols can also be present in non-negligible amounts during this time period.

Smoke from biomass fires is dominated by submicron-sized particles, frequently containing internally mixed black carbon (Reid et al., 2005, Li et al., 2003), and produces low PDR and high S_a at 532 nm (Müller et al., 2007; Omar et al., 2009; Burton et al., 2013). Smoke S_a and PDRs can vary depending on the type of fire, the combustion source and the age of the smoke. The S_a values retrieved in this study are consistent with the case study presented in Hu et al. (2007) that used the OWC constrained technique and obtained a S_a of 66±6 sr for a smoke layer transported from the southern Africa biomass burning region. Our retrieved values are also consistent with values retrieved during the SAFARI 2000 field campaign in northeastern South Africa. Values of 50 – 90 sr were retrieved from micro-pulse lidar observations of dense smoke (Campbell et al., 2003) and, in cases where the column AOD was dominated by smoke, values of 70-74 sr were obtained by combining airborne backscatter lidar data with ground-based sunphotometer data (McGill et al., 2003).

The PDR values retrieved in the smoke region are typically smaller than 0.1, with mean/median/mode values of 0.043/0.036/0.041±0.64 for all smoke layers analyzed and 0.038/0.036/0.041±0.026 for the layers with ASR > 0.2. Irrespective of aerosol type, the PDR calculation can be biased significantly by noise when the aerosol layer is weakly scattering. The standard deviation computed from all the analyzed smoke layers is large (0.64), but is reduced to

0.026 when weakly scattering layers are screened out. The PDR distributions appear to be non-Gaussian with a positive skewness. Internally mixed potassium salts and organic particles are the predominant components in the smoke from the African biomass burning, and the smoke particles undergo hygroscopic growth, reaction and transformation (Reid et al., 2005). Although dominated by fine mode particles, large complex chain-like soot aggregates and aggregates of fine particles have been observed in the smoke from the biomass burning in the southern Africa (Li et al., 2003). Unlike the surrounding fine mode particles, these large nonspherical particles can strongly depolarize the incident photons and the depolarization ratio of measured backscatter signals from smoke varies depending on the fraction of nonspherical particles (Martins et al., 1998; Murayama et al., 2004; Sun et al., 2013).

The OWC smoke retrieval compares well with the urban/smoke category measured by HSRL during the Caribbean 2010 campaign shown in Fig. 9b. Although the distribution for the urban/smoke category is complex because of the mixing with marine and dust, the mode values for S_a and PDR are ~69.5 sr and ~0.025, respectively, consistent with the OWC retrieved mode values.

4.4 CALIOP L2 AOD Evaluation

In this subsection, we attempt to evaluate above-cloud AOD produced by the CALIOP L2 standard retrieval and estimate an error budget based on the analysis of the two selected regions. Figures 11 and 12 present comparisons of the analysis results where the OWC retrieval is considered to be 'truth'. For the dust transport region, as shown in Fig. 11a, the majority of $\mathrm{AOD_{L2}}$-$\mathrm{AOD_{OWC}}$ scatters falls on a line with a slop of ~0.75 (the fit curve is not shown). The mean value for $\mathrm{AOD_{L2}}$ is 0.183 (Fig. 11f), which is 25.9% smaller than the mean value of $\mathrm{AOD_{OWC}}$ (0.247). We examine the factors that may contribute to this discrepancy and estimate an error budget. In the L2 retrieval, the lidar ratio sometimes needs to be adjusted when the retrieval diverges and becomes unstable (Young and Vaughan, 2009). Such cases rarely occur in the dust region (~2.5% of the retrievals), and are hereafter excluded to simplify the remaining analysis. The CALIOP aerosol classification (Fig. 11e) is dominated by “dust” (contributing 91.4% of the total AOD), followed by “polluted dust” (8.5%), consistent with expectations for the area. Assuming that any aerosol type in this region other than “dust” is a misclassification, rescaling the extinction of all non-“dust” range bins using Eq. (3) decreases the AOD only by 0.006. This accounts for only 9.4% of the AOD discrepancy. This small change indicates that the CALIOP L2 algorithms have been largely successful in correctly identifying the above-cloud aerosol type as “dust” in this region.

As mentioned earlier, the FC retrieval using a fixed S_a can provide insight into the error due to the failure of the L2 algorithms to detect the full vertical extent of aerosol layers. The mean AOD from the FC retrieval using the modeled $S_{a,model}$ value (40 sr) for “dust” ($AOD_{FC, model}$) is 0.202, which is larger than that for the rescaled L2 AOD ($AOD_{L2, rescaled} = 0.177$) by 0.025, but still smaller than AOD_{OWC} by 0.045. We note that $AOD_{L2, res}$ was derived by scaling all other aerosol types to “dust” using Eq. (3). Therefore, the difference between $AOD_{FC, mod}$ and $AOD_{L2,rescaled}$ is mainly due to the failure to detect the full extent of the aerosol layers (e.g., due to inherent detection limits). The failure to detect those parts of the aerosol layer(s) that lie below the CALIOP detection limit may contribute under half (39.1%; see Tables 1 and 2) of the total AOD discrepancy. From Fig. 11d we can see that the difference between $AOD_{L2,rescaled}$ and $AOD_{FC,model}$ comes mainly from the extinction retrieval at lower altitudes. Below 1 km there may be some contamination by cloud edges. Although the L2 algorithms fail to detect the aerosol above about 7km (Fig. 11d), the aerosol loading here is very small and does not contribute significantly to the column AOD. Small differences between the L2 and FC profiles below 2 km indicate the L2 algorithms are doing a moderately good job of detecting the base of the dust layer. The standard CALIOP modeled $S_{a,model}$ for dust (40 sr) is ~10% smaller than the OWC retrieved value (Fig. 8c). Differences in S_a have a nonlinear effect on the retrieved AOD, and thus this 10% disparity in S_a contributes the majority (70.3%) of the total AOD discrepancy, so that, in the mean, AOD_{L2} underestimates AOD_{OWC} by 18.6%. Table 1 compares all AOD retrievals for the dust transport region. Table 2 shows the error budget estimated for AOD_{L2} in the dust transport regions along with the error budget in the smoke transport region that will be discussed in the next paragraph.

In the smoke transport region, the L2 AOD retrieval is not as successful as in the dust transport region. There are two branches in the AOD_{L2}-AOD_{OWC} distribution (Fig. 12a). As seen in Fig. 12f and Table 3, the L2 smoke AOD is 0.191, which is smaller than the smoke AOD_{OWC} (0.311) by 38.6%. As seen in Fig. 12e, the dominant aerosol type in the region, as classified in the CALIOP L2 product, is “smoke” (83.3% by AOD), which is expected. The next most common type is “polluted dust” (8.4%), followed by “marine” (4.5%) and “polluted continental (3.9%). “Polluted dust” is possible for this area. However, “marine” aerosols are unlikely to be found above the boundary clouds in this region, and these misclassifications have been traced to a coding error within the aerosol subtyping module. Rescaling the extinction coefficients of those aerosols classified as types other than “smoke” increases the mean AOD by 0.031 to 0.222, which corresponds to 25.8% of the total AOD discrepancy. The lower branch in the AOD_{L2}-AOD_{OWC} distribution disappear almost entirely after the rescaling, indicating that the lower branch is due mainly to the subtyping error.

$AOD_{FC,moddel}$ for the FC retrieval using a modeled $S_{a,model}$ of 70 sr for “smoke” is 0.314, larger than the OWC AOD by only 1%. This implies that a failure to detect the full extent of the aerosol layers lying above the clouds, whether due to inherent detection limits or algorithm deficiencies, is responsible for 76.7% of the AOD discrepancy. The FC retrievals suggest that the L2 layer detection scheme detects the upper parts of the smoke layers fairly well, but fails to detect a significant fraction of the aerosol below ~3 km (Fig. 12d). Smoke aerosols typically have large absorption at visible wavelengths, which increases detection difficulties as the signal penetrates into the lower part of a layer (also see the example in Figs. 4 and 5). Misdetection of aerosol layer bases, and to a lesser extent layer tops, thus appears to be the main cause for the AOD differences for the case of smoke above opaque clouds.

The S_a values retrieved using AOD_{OWC} as a constraint have a mean/median/mode value of 74.8/71.8/69.8±17 sr for the screened smoke data. The modeled $S_{a,model}$ value of 70 sr (Omar et al., 2009) thus appears to be appropriate and representative for the transported smoke when compared with the OWC-constrained S_a (Fig. 12f). While the mean values for AOD_{OWC} and $AOD_{FC,\ model}$ are very close, AOD_{OWC} appears to be a little bit larger than $AOD_{FC,\ model}$ for smaller AODs and somewhat smaller for larger AODs (Figs. 12c and 12f).

The above-cloud aerosol cases evaluated by Kacenelenbogen et al. (2014) were generally optically thin and observed mostly during daytime. Under these conditions, failure to detect the full extent of entire layer of aerosols is a major cause of errors, as the signal levels from these tenuous aerosol layers frequently lie below the detection limit of the layer finding algorithm. As a result, the CALIOP standard data processing can sometimes substantially underestimate the daytime occurrence frequency of aerosol.

4.5 Further Comments about Dust Lidar Ratio

To help evaluate CALIOP AOD retrievals, comparison studies have been performed using AERONET measurements (e.g., Amiridis et al., 2013, Schuster et al., 2012) and ground-based

Raman lidar measurements (e.g., Tesche et al., 2013). These comparison studies have provided many details useful for a better understanding of the CALIOP AOD retrieval uncertainties. In general, these studies show that the CALIOP V3 retrievals typically underestimate dust AODs, and are in general agreement with the results presented in this work. Wandinger et al. (2010), Amiridis et al. (2013), and Tesche et al. (2013) found that the CALIOP retrieved dust backscatter is in good agreement with the ground-based measurements near the source and in Europe but the retrieved dust extinction is underestimated. These authors have suggested using a dust lidar ratio of 56–58 sr, along with the appropriate correction for multiple scattering in order to produce an extinction retrieval which would provide the best match to the AERONET and/or ground-based lidar measurements in their selected spatial domains. In this section we show that, because of the nonlinear dependence of the AOD retrieval on lidar ratio (Winker et al., 2009 and Young et al., 2013), an increase of ~10% in the lidar ratio will increase the retrieved AOD by ~ 26% and thus match the derived OWC AOD. The following relationship between the error in AOD and error in S_a is given in Winker et al. (2009),

$$\Delta\tau = \frac{\left(e^{2\tau'}-1\right)}{2}\frac{\Delta S_a}{S_a} = \frac{\left(e^{2(\tau+\Delta\tau)}-1\right)}{2}\frac{\left(S_a'-S_a\right)}{S_a}, \qquad (8)$$

where $\tau' = \tau + \Delta\tau$ is the retrieved AOD and τ is the true AOD, S_a is the aerosol lidar ratio and S_a' is the lidar ratio used in the retrieval. For small optical depths, the relative error in optical depth is roughly proportional to the relative error in lidar ratio, $\Delta\tau/\tau = \Delta S_a/S_a$. As the optical depth increases, the relative error in optical depth increases faster than that in lidar ratio. We note that while Eq. (8) was originally derived under assumption that the aerosol layer is dense or moderately dense, it appears to be equally applicable throughout the whole parameter space considered in this paper. A more rigorous analysis of extinction error propagation and parameter sensitivities can be found in Young et al. (2013).

Figure 13 presents 2D distributions of FC-retrieved AODs using S_a = 40, 45, 50, 55 and 60 sr versus OWC-retrieved AODs for the same dataset for the dust transport region (JJA 2007-2012), along with the corresponding extinction profiles. The blue lines in panels (a) – (e) indicate the relation expected for a linear scaling, with a slope of $S_a / S_{a,OWC}$. The broken red lines represent the AOD, $\tau' = \tau + \Delta\tau$, numerically calculated using Eq. (8). Approximately 10 iterations are required in the calculation to solve for $\Delta\tau$, which appears on both sides of Eq. (8). It is seen from Fig. 13

that, the FC-OWC AOD distribution generally falls on the linear scaling line for the case of S_a=45 sr which is very close to the retrieved value (44.4 sr) or the cases for smaller AOD values. Significant deviation of the FC-OWC AOD distribution from the linear scaling line starts to occur in the S_a=50 sr case, for example, when OWC AOD ~ 0.4. Such a nonlinear behavior becomes more significant and the retrieval becomes unstable more frequently as S_a increases.

Nonlinear behavior is also seen in the extinction profiles (Fig. 13f). The effect of a larger lidar ratio on the retrieved extinction profile increases more and more as the retrieval proceeds from top to bottom. In the FC retrievals, the correction for attenuation during the lidar signal inversion is terminated when the retrieved AOD is unreasonably large (e.g., > 5) to prevent the retrieval blowing up. For this reason, the FC extinction using S_a=60 sr is smaller than that using S_a=55 sr below ~0.7 km.

Figure 14 shows the mean AOD_{FC} retrieved using different S_a values as a function of S_a. The corresponding data are listed in Table 4. It is clear that the AOD retrieval is not linearly dependent on S_a. For the FC retrieval using S_a=50 sr, for example, although S_a is increased by 25% compared with the retrieval using the CALIOP modeled value of $S_{a,\text{model}}$=40 sr, the retrieved mean AOD is increased by 66%, ~2.6 times the S_a increase. Therefore, for a more accurate estimate of S_a from the AOD ratio, the nonlinear dependence of AOD on S_a must be taken into account. We note that the S_a and AOD retrieved in this study are effective quantities which have not been corrected for potential effects of multiple scattering. To derive conventional values, consistent with airborne HSRL or AERONET measurements, S_a and AOD should be corrected (i.e., divided by) the appropriate multiple scattering factor, η. Simulations show that the multiple scattering factor is generally around 0.9 – 0.95 for moderately dense dust layers (Liu et al., 2011) and can decrease to 0.8 – 0.85 for very dense cases (extinction coefficient > ~2 km^{-1}), although the appropriate value of η depends on particle size and the geometric thickness of the dust layer (Winker 2003).

5. Summary

Validating all aspects of the CALIOP data products is an ongoing task for the CALIPSO team. In this paper, we evaluated CALIOP retrievals of aerosols above water cloud during nighttime, for which comparison data from independent sensors such as MODIS and AERONET are not currently available. We focused on two spatial domains, one along the African dust transport pathway over the North Atlantic and the second over the African smoke transport pathway across the South Atlantic. Six years of CALIOP data were analyzed. The analysis was limited to cases where opaque water clouds (OWCs) were present below the aerosol layers so that the OWC constrained retrieval technique could be used. In the standard CALIOP aerosol extinction retrieval, S_a is assigned on a layer-by-layer basis by a scene classification algorithm that determines the most likely aerosol type for each layer. The layer extinction profile and AOD are then retrieved using the mean S_a that characterizes the assigned aerosol type. When using this technique, a certain amount of AOD error is inevitable, simply because the lidar ratios within each aerosol type can have a fairly wide range of natural variability (e.g., ±50% for the CALIOP V3 dust model). The derived AOD estimates will be in error whenever the model mean S_a is insufficiently close to the actual S_a of the aerosol layer. On the other hand, the OWC method allows direct retrieval of lidar ratios, and thus enables measurement-based evaluation and improvement of the standard CALIOP aerosol models and retrieval techniques.

In assessing the CALIOP lidar ratio models, the values obtained using the OWC-constrained technique are reasonably consistent (to within ~10%) with the CALIOP V3 model value for pure dust (40 ± 20 sr), and essentially identical to the CALIOP model value for biomass burning aerosol (70 ± 28 sr). For layers detected by the L2 processing within the dust transport region, the mean/median values for the full set of OWC-retrieved lidar ratios are 50.5/45.5 ± 26.4 sr. For the subset of aerosol layers having mean aerosol attenuated scattering ratios (ASR) above 0.3, the mean/median values are 45.1/44.4 ± 8.8 sr. For smoke detected within the smoke transport region, the mean/median lidar ratios are 69.6/71.8 ± 26.5 sr for all layers and 69.4/70.4 ± 16.2 sr for layers having ASR > 0.2.

Particulate depolarization ratios were also examined. The median dust PDR is 0.277 ± 4.24 for the full dust data set, and 0.281 ± 0.044 sr for all those dust layers with ASR > 0.3. The corresponding PDR for smoke is 0.036 ± 0.64 for all smoke layers and 0.036 ± 0.026 for smoke layers having ASR > 0.2

When comparing the AOD reported in the CALIPSO Level 2 data products to the OWC-retrieved AOD, the retrieved L2 AOD underestimates the measured OWC AOD by 25.9% in the dust transport region (0.183 for L2 vs. 0.247 for OWC). When partitioning the errors into a comprehensive error budget we find that the CALIOP aerosol subtyping algorithm performs well in the dust region during nighttime: 91.4% of all layers are classified as “dust”, with an additional

8.5% of layers being classified as “polluted dust”. Misclassification of aerosol subtype is thus responsible for a 9.4% (overestimate) of the total discrepancy between the L2 and OWC retrievals, which compensates somewhat for the underestimates caused by other error sources. Failure to detect the full geometric extent of the dust layers is responsible for -39.1% (negative sign indicating an underestimate) of the error budget. The largest contributor to the L2 underestimate of dust AOD is due to the difference between the CALIOP modeled dust lidar ratio and the OWC measured values. While the L2-modeled and OWC-measured lidar ratio values are different by only ~10%, the nonlinear relationship between S_a and AOD results in lidar ratio differences being the root cause for -70.3% of the L2 AOD underestimation.

The L2 aerosol retrieval generates a more substantial underestimate of AOD in the smoke transport region. The AOD underestimate is 38.6% in the smoke transport region (0.191 for L2 vs. 0.311 for OWC), larger than that in the dust transport region. However, in the smoke region the differences between the L2-modeled and OWC-measured lidar ratios are negligible, thus make no meaningful contribution to the overall error budget (i.e., an overestimate of ~2.5%). Possible misclassification of aerosol subtype accounts for -25.8% and the layer detection failure contributes the most (-76.7%) to the underestimation of the L2 smoke AOD.

Acknowledgements:

We are very grateful to the NASA Langley Research Center’s HSRL team for providing the HSRL measurement data and Dr. Stuart Young for the constructive discussions regarding the error sensitivity analysis of the lidar signal inversion. We also thank two anonymous reviewers and three colleagues for the many useful suggestions and comments, which have significantly improved this paper. The CALIPSO data used in this paper were obtained from the NASA Langley Atmospheric Sciences Data Center.

References

Amiridis, V., Wandinger, U., Marinou, E., Giannakaki, E., Tsekeri, A., Basart, S., Kazazis, S., Gkikas, A., Taylor, M., Baldasano, J., Ansmann, A.: Optimizing CALIPSO Saharan dust retrievals, Atmos. Chem. Phys., 13, 12089–12106, 2013.

Burton, S. P., Ferrare, R. A., Hostetler, C. A., Hair, J. W., Rogers, R. R., Obland, M. D., Butler, C. F., Cook, A. L., Harper, D. B., and Froyd, K. D.: Aerosol classification using airborne High

Spectral Resolution Lidar measurements – methodology and examples, Atmos. Meas. Tech., 5, 73–98, doi:10.5194/amt-5-73-2012, 2012.

Burton, S. P., Ferrare, R. A., Vaughan, M. A., Omar, A. H., Rogers, R. R., Hostetler, C. A., and Hair J. W.: Aerosol classification from airborne HSRL and comparisons with the CALIPSO vertical feature mask, Atmos. Meas. Tech., 6, 1397–1412, 2013.

Campbell, J. R., Welton, E. J., Spinhirne, J. D., Ji, Q., Tsay, S. C., Piketh, S. J., Barenbrug, M., and Holben, B. N.: Micropulse lidar observations of tropospheric aerosols over north-eastern South Africa during the ARREX and SAFARI 2000 dry season experiments, J. Geophys. Res.-Atmos., 108, 8497, doi:10.1029/2002jd002563 , 2003.

Carlson, T. N., and Prospero J. M.: The large-scale movement of Saharan air outbreaks over the northern equatorial Atlantic, J. Appl. Meteorol., 11, 283–297, 1972.

Cattrall, C., Reagan, J., Thome, K., and Dubovik, O.: Variability of aerosol and spectral lidar and backscatter and extinction ratios of key aerosol types derived from selected Aerosol Robotic Network locations, J. Geophys. Res., 110, D10S11, doi:10.1029/2004JD005124, 2005.

Chand, D., Wood, R., Anderson, T. L., Satheesh, S. K., and Charlson, R. J.: Satellite-derived direct radiative effect of aerosols dependent on cloud cover, Nat. Geoscience, 2, 181-184, 2009.

Climate Change 2013: The Physical Science Basis. Contribution of Working Group I to the Fifth Assessment Report of the Intergovernmental Panel on Climate Change, edited by: Stocker, T. F., Qin, D., Plattner, G.-K., Tignor, M., Allen, S. K., Boschung, J., Nauels, A., Xia, Y., Bex, V., and Midgley, P. M., Cambridge University Press, Cambridge, UK and New York, NY, USA, 1535 pp., 2013.

Cook, J., and Highwood, E. J.: Climate response to tropospheric absorbing aerosol in an intermediate general-circulation model, Q. J. Roy. Meteor. Soc., 130, 175–191, 2004.

Cooke, W., Koffi, B., and Cregoire, J. M.: Seasonality of vegetation firs in African from remote sensing data and application to a global chemistry model, J. Geophys. Res., 101, 21051–21065, 1996.

Elterman, L.: Aerosol measurements in the troposphere and stratosphere. Appl. Opt., 5, 1769–1776, 1966.

Esselborn, M., Wirth, M., Fix, A., Weinzierl, B., Rasp, K., Tesche, M., and Petzold, A.: Spatial distribution and optical properties of Saharan dust observed by airborne high spectral resolution lidar during SAMUM 2006, Tellus B, 61, 131–143, doi:10.1111/j.1600-0889.2008.00394.x, 2009.

Fernald, F. G.: Analysis of atmospheric lidar observations: some comments, App. Opt., 23, 652-653, 1984.

Freudenthaler, V., Esselborn, M., Wiegner, M., Althausen, D., Wirth, M., Fix, A., Ehret, G., Knippertz, P., Toledano, C., Gasteiger, J., Garhammer, M., and Seefeldne, M.: Depolarization ratio profiling at several wavelengths in pure Saharan dust during SAMUM 2006, Tellus B, 61, 165–79, 2009.

Hair, J. W., Hostetler, C. A., Cook, A. L., Harper, D. B., Ferrare, R. A., Mack, T. L., Welch, W., Izquierdo, L. R., and Hovis, F. E.: Airborne High Spectral Resolution Lidar for profiling aerosol optical properties, Appl. Optics, 47, 6734–6752, doi:10.1364/AO.47.006734, 2008.

Hansen, J., Sato, M., and Ruedy, R.: Radiative forcing and climate response, J. Geophys. Res., 102(D6), 6831-6864, 1997.

Haywood, J. M., Pelon, J., Formenti, P., Bharmal, N., Brooks, M., Capes, G., Chazette, P., Chou, C., Christopher, S., Coe, H., Cuesta, J., Derimian, Y., Desboeufs, K., Greed, G., Harrison, M., Heese, B., Highwood, E. J., Johnson, B., Mallet, M., Marticorena, B., Marsham, J., Milton, S., Myhre, G., Osborne, S. R., Parker, D. J., Rajot, J.-L., Schulz, M., Slingo, A., Tanre, D., and Tulet, P.: Overview of the dust and biomass-burning experiment and African monsoon multidisciplinary analysis special observing period-0, J. Geophys. Res., 113, D00C17, doi:10.1029/2008JD010077, 2008.

Hu, Y., Vaughan, M., Liu, Z., Powell, K., and Rodier, S.: Retrieving optical depths and lidar ratios for transparent layers above opaque water clouds from CALIPSO lidar measurements, IEEE Trans. Geosci. Remote Sens. Lett., 4, 523–526, 2007.

Hu, Y., Vaughan, M., Winker, D., Liu, Z., Noel, V., Bissonnette, L., Roy, G., McGill, M., and Trepte, C.: A simple multiple scattering-depolarization relation of water clouds and its potential applications, Proceedings of 23nd International Laser Radar Conference, Nara, Japan, 19-22, 2006.

Hu, Y., Winker, D., Vaughan, M., Lin, B., Omar, A., Trepte, C., Flittner, D., Yang, P., Sun, W., Liu, Z., Wang, Z., Young, S., Stamnes, K., Huang, J., Kuehn, R., Baum, B., and Holz, R.:

CALIPSO/CALIOP Cloud Phase Discrimination Algorithm, J. Atmos. Oceanic Technol., 26, 2293-2309, 2009.

Hu, Y.: Depolarization ratio–effective lidar ratio relation: Theoretical basis for space lidar cloud phase discrimination, Geophys. Res. Lett., 34, L11812, doi:10.1029/2007GL029584, 2007.

Huneeus, N., Schulz, M., Balkanski, Y., Griesfeller, J., Prospero, J., Kinne, S., Bauer, S., Boucher, O., Chin, M., Dentener, F., Diehl, T., Easter, R., Fillmore, D., Ghan, S., Ginoux, P., Grini, A., Horowitz, L., Koch, D., Krol, M. C., Landing, W., Liu, X., Mahowald, N., Miller, R., Morcrette, J.-J., Myhre, G., Penner, J., Perlwitz, J., Stier, P., Takemura, T., and Zender, C. S.: Global dust model intercomparison in AeroCom phase I, Atmos. Chem. Phys., 11, 7781–7816, doi:10.5194/acp-11-7781-2011, 2011.

Jethva, H., Torres, O., Remer, L. A., and Bhartia, P. K.: A color ratio method for simultaneous retrieval of aerosol and cloud optical thickness of above-cloud absorbing aerosols from passive sensors: Application to MODIS measurements, IEEE Trans. Geosci. Remote Sens., 51, 3862–3870, doi:10.1109/TGRS.2012.2230008, 2013.

Kacenelenbogen, M., Redemann, J., Vaughan, M. A., Omar, A. H., Russell, P. B., Burton, S., Rogers, R. R., Ferrare, R. A., and Hostetler, C. A.: An evaluation of CALIOP/CALIPSO's aerosol-above-cloud detection and retrieval capability over North America, J. Geophys. Res. Atmos., 119, 230–244, doi:10.1002/2013JD020178, 2014.

Kanitz, T., Engelmann, R., Heinold, B., Baars, H., Skupin, A., and Ansmann, A.: Tracking the Saharan Air Layer with shipborne lidar across the tropical Atlantic, Geophys. Res. Lett., 41, doi:10.1002/2013GL058780, 2014.

Karyampudi, V. M., Palm, S. P., Reagen, J. A., Fang, H., Grant, W. B., Hoff, R. M., Moulin, C., Pierce, H. F., Torres, O., Browell, E. V., and Melfi, S. H.: Validation of the Saharan Dust Plume Conceptual Model using lidar, meteosat, and ECMWF data, B. Am. Meteorol. Soc., 80, 1045–1075, 1999

Kim, M. H., Kim, S. W., Yoon, S. C., and Omar A. H.: Comparison of aerosol optical depth between CALIOP and MODIS-Aqua for CALIOP aerosol subtypes over the ocean, J Geophys Res-Atmos, 118(23), 13241-13252, 2013.

Kinne, S., Schulz, M., Textor, C., Guibert, S., Balkanski, Y., Bauer, S. E., Berntsen, T., Berglen, T. F., Boucher, O., Chin, M., Collins, W., Dentener, F., Diehl, T., Easter, R., Feichter, J., Fillmore, D., Ghan, S., Ginoux, P., Gong, S., Grini, A., Hendricks, J., Herzog, M., Horowitz, L., Isaksen, I., Iversen, T., Kirkevåg, A., Kloster, S., Koch, D., Kristjansson, J. E., Krol, M., Lauer, A., Lamarque, J. F., Lesins, G., Liu, X., Lohmann, U., Montanaro, V., Myhre, G., Penner, J., Pitari, G., Reddy, S., Seland, O., Stier, P., Takemura, T., and Tie, X.: An AeroCom initial assessment – optical properties in aerosol component modules of global models, Atmos. Chem. Phys., 6, 1815–1834, doi:10.5194/acp-6-1815-2006, 2006.

Kittaka, C., Winker, D. M., Vaughan, M. A., Omar, A., and Remer, L. A.: Intercomparison of column aerosol optical depths from CALIPSO and MODIS-Aqua, Atmos. Meas. Tech., 4, 131–141, doi:10.5194/amt-4-131-2011, 2011.

Koffi, B., Schulz, M., Breon, F.-M., Griesfeller, J., Griesfeller, J., Winker, D., Balkanski, Y., Bauer, S., Berntsen, T., Chin, M., Collins, W. D., Dentener, F., Diehl, T., Easter, R., Ghan, S., Ginoux, P., Gong, S., Horowitz, L. W., Iversen, T., Kirkevag, A., Koch, D., Krol, M., Myhre, G., Stier, P., and Takemura, T.: Application of the CALIOP layer product to evaluate the vertical distribution of aerosols estimated by global models: AeroCom phase I results, J. Geophys. Res., 117, D10201, doi:10.1029/2011JD016858, 2012.

Levine, J. S., Coffer III, W. R., Cahoon Jr., D. R., and Winstead, El. L.: A driver for global change, Environ. Sci. Technol., 29(3), 120-125, 1995.

Li, J., Posfai, M., Hobbs, P. V., and Buseck, P. R.: Individual aerosol particles from biomass burning in southern Africa: 2. Compositions and aging of inorganic particles, J. Geophys. Res., 108(D13), 8484, doi:10.1029/2002JD002310, 2003.

Liu, D., Z. Wang, Z. Liu, D. M .Winker, and C. Trepte: A height resolved global view of dust aerosols from the first year CALIPSO lidar measurements, J. Geophys. Res., 113, D16214, doi:10.1029/2007JD009776, 2008.

Liu, Z., Omar, A., Vaughan, M., Hair, J., Kittaka, C., Hu, Y., Powell, K., Trepte, C., Winker, D., Hostetler, C., Ferrare, R., and Pierce, R.: CALIPSO lidar observations of the optical properties of Saharan dust: A case study of long-range transport, J. Geophys. Res., 113, D07207, doi:10.1029/2007JD008878, 2008.

Liu, Z., Vaughan, M. A., Winker, D. M., Kittaka, C., Getzewich, B. J., Kuehn, R. E., Omar, A., Powell, K., Trepte, C. R., and Hostetler, C. A.: The CALIPSO Lidar Cloud and Aerosol Discrimination: Version 2 Algorithm and Initial Assessment of Performance, J. Atmos. Oceanic Technol., 26, 1198–1213, doi:10.1175/2009JTECHA1229.1, 2009.

Liu, Z., Winker, D., Omar, A., Vaughan, M., Trepte, C., Hu, Y., Powell, K., Sun, W., and Lin, B.: Effective lidar ratios of dense dust layers over North Africa derived from the CALIOP measurements, J. Quant. Spectrosc. Ra., 112, 204–213, doi:10.1016/j.jqsrt.2010.05.006, 2011.

Lopes, F. J. S., Landulfo, E., and Vaughan, M. A.: Evaluating CALIPSO’s 532 nm lidar ratio selection algorithm using AERONET sun photometers in Brazil, Atmos. Meas. Tech., 6, 3281–3299, doi:10.5194/amt-6-3281-2013, 2013.

Maring, H., D. L. Savioe, M. A. Izaguirre, L. Custals, and J. S. Reid, Mineral dust aerosol size distribution change during atmospheric transport, J. Geophys. Res., 108(D19), 8592, doi:10.1029/2002JD002536, 2003.

Martins, J. V., Hobbs P. V., Weiss, R. E., and Artaxo, P.: Sphericity and morphology of smoke particles from biomass burning in Brazil, J. Geophys. Res., 103(D24), 32,051–32,057, 1998.

McGill, M. J., Hlavka, D. L., Hart, W. D., Welton, E. J., and Campbell, J. R.: Airborne lidar measurements of aerosol optical properties during SAFARI-2000, J. Geophys. Res., 108, 8493, doi:10.1029/2002JD002370, 2003.

Miles, N. J., Verlinde, J., and Clothiaux E. E.: Cloud droplet size distributions in low-level stratiform clouds, J. Atmos. Sci., 57, 295–311, 2000.

Muller, D., Ansmann, A., Mattis, I., Tesche, M., Wandinger, U., Althausen, D., and Pisani, G.: Aerosol-type-dependent lidar ratios observed with Raman lidar, J. Geophys. Res.-Atmos., 112, D16202, doi:10.1029/2006jd008292, 2007.

Murayama, T., Muller, D., Wada, K., Shimizu, A., Sekiguchi, M., and Tsukamoto, T.: Characterization of Asian dust and Siberian smoke with multi-wavelength Raman lidar over Tokyo, Japan in spring 2003, Geophys. Res. Lett., 31, doi:10.1029/2004gl021105, 2004.

O’Connor, E. J., Illingworth, A. J., and Hogan, R. J.: A technique for autocalibration of cloud lidar, J. Atmos. Ocean. Tech., 21, 777–786, 2004.

Omar, A. H., Winker, D. M., Tackett, J., Giles, D., Kar, J., Liu, Z., Vaughan, M., Powell, K., and Trepte, C.: CALIOP and AERONET aerosol optical depth comparisons: one size fits none, J. Geophys. Res., 118, 4748–4766, doi:10.1002/jgrd.50330, 2013.

Omar, A., Liu, Z., Vaughan, M., Thornhill, K. L., Kittaka, C., Ismail, S., Hu, Y., Chen, G., Winker, D., Trepte, C., Winstead, E. L., and Anderson, B. E.: Extinction-to-backscatter ratios of Saharan dust layers derived from in situ measurements and CALIPSO overflights during NAMMA, J. Geophys. Res., 115, D24217, doi:10.1029/2010JD014223, 2010.

Omar, A., Winker, D., Kittaka, C., Vaughan, M., Liu, Z., Hu, Y., Trepte, C., Rogers, R., Ferrare, R., Kuehn, R., and Hostetler, C.: The CALIPSO Automated Aerosol Classification and Lidar Ratio Selection Algorithm, J. Atmos. Oceanic Technol., 26, 1994–2014, doi:10.1175/2009JTECHA1231.1, 2009.

Pinnick, R. G., Jennings, S. G., Chylek, P., Ham, C., and Grandy Jr., W. T.: Backscatter and extinction in water clouds, J. Geophys. Res., 88, 6787–6796, 1983.

Platt, C. M. R.: Lidar and radiometric observations of cirrus clouds. J. Atmos. Sci., 30, 1191-1204, 1973.

Powell, K. A., Hostetler, C. A., Liu, Z., Vaughan, M. A., Kuehn, R. E., Hunt, W. H., Lee, K., Trepte, C. R., Rogers, R. R., Young, S. A., and Winker, D. M.: CALIPSO lidar calibration algorithms: Part I – Nighttime 532 nm parallel channel and 532 nm perpendicular channel, J. Atmos. Ocean. Tech., 26, 2015–2033, 2009.

Redemann, J., Vaughan, M. A., Zhang, Q., Shinozuka, Y., Russell, P. B., Livingston, J. M., Kacenelenbogen, M., and Remer, L. A.: The comparison of MODIS-Aqua (C5) and CALIOP (V2 & V3) aerosol optical depth, Atmos. Chem. Phys., 12, 3025–3043, doi:10.5194/acp-12-3025-2012, 2012.

Reid, J. S., Kappmann, R., Eck, T. F., and Eleuterio, D. P.: A review of biomass burning emissions part II: intensive physical properties of biomass burning particles, Atmos. Chem. Phys., 5, 799–825, doi:10.5194/acp-5-799-2005, 2005.

Rogers, R. R., Hostetler, C. A., Hair, J.W., Ferrare, R. A., Liu, Z., Obland, M. D., Harper, D. B., Cook, A. L., Powell, K. A., Vaughan, M. A., and Winker, D. M.: Assessment of the CALIPSO

Lidar 532nm attenuated backscatter calibration using the NASA LaRC airborne High Spectral Resolution Lidar, Atmos. Chem. Phys., 11, 1295–1311, 2011.

Sakaeda, N., Wood, R., and Rasch, P. J.: Direct and semidirect aerosol effects of southern African biomass burning aerosol, J. Geophys. Res., 116, D12205, doi:10.1029/2010JD015540, 2011.

Sassen, K., and Cho, B. S.: Subvisual thin cirrus lidar dataset for satellite verification and climatological research. J. Appl. Meteor., 31, 1275–1285, 1992.

Schulz, M., Textor, C., Kinne, S., Balkanski, Y., Bauer, S., Berntsen, T., Berglen, T., Boucher, O., Dentener, F., Guibert, S., Isaksen, I. S. A., Iversen, T., Koch, D., Kirkevåg, A., Liu, X., Montanaro, V., Myhre, G., Penner, J. E., Pitari, G., Reddy, S., Seland, Ø., Stier, P., and Takemura, T.: Radiative forcing by aerosols as derived from the AeroCom present-day and pre-industrial simulations, Atmos. Chem. Phys., 6, 5225–5246, doi:10.5194/acp-6-5225-2006, 2006.

Schuster, G. L., Vaughan, M., MacDonnell, D., Su, W., Winker, D., Dubovik, O., Lapyonok, T., and Trepte, C.: Comparison of CALIPSO aerosol optical depth retrievals to AERONET measurements, and a climatology for the lidar ratio of dust, Atmos. Chem. Phys., 12, 7431-7452, doi:10.5194/acp-12-7431-2012, 2012.

Sun, W., Liu, Z., Videen, G., Fu, Q., Muinonen, K., Winker, D. M., Lukashin, C., Jin, Z., Lin, B., and Huang, J.: For the depolarization of linearly polarized light by smoke particles, J. Quant. Spectrosc. Ra., 122, 233–237, doi:10.1016/j.jqsrt.2012.03.031, 2013.

Tesche, M., Ansmann, A., M¨uller, D., Althausen, D., Mattis, I., Heese, B., Freudenthaler, V., Wiegner, M., Esselborn, M., Pisani, G., and Knippertz, P.: Vertical profiling of Saharan dust with Raman lidars and airborne HSRL in southern Morocco during SAMUM, Tellus B, 61, 144–164, doi:10.1111/j.1600- 0889.2008.00390.x, 2009.

Tesche, M., Wandinger, U., Ansmann, A., Althausen, D., Müller, D., and Omar, A. H.: Ground-based validation of CALIPSO observations of dust and smoke in the Cape Verde region, J. Geophys. Res., 118, 1–14, doi:10.1002/jgrd.50248, 2013.

Textor, C., Schulz, M., Guibert, S., Kinne, S., Balkanski, Y., Bauer, S., Berntsen, T., Berglen, T., Boucher, O., Chin, M., Dentener, F., Diehl, T., Easter, R., Feichter, H., Fillmore, D., Ghan, S., Ginoux, P., Gong, S., Grini, A., Hendricks, J., Horowitz, L., Huang, P., Isaksen, I., Iversen, I., Kloster, S., Koch, D., Kirkevåg, A., Kristjansson, J. E., Krol, M., Lauer, A., Lamarque, J. F., Liu, X., Montanaro, V., Myhre, G., Penner, J., Pitari, G., Reddy, S., Seland, Ø., Stier, P., Takemura, T., and Tie, X.: Analysis and quantification of the diversities of aerosol life cycles within AeroCom, Atmos. Chem. Phys., 6, 1777–1813, doi:10.5194/acp-6-1777-2006, 2006.

Torres, O., Ahn, C., and Chen, Z.: Improvements to the OMI near UV aerosol algorithm using A-train CALIOP and AIRS observations, Atmos. Meas. Tech., 6, 5621-5652, doi:10.5194/amtd-6-5621-2013, 2013.

Torres, O., Jethva, H., and Bhartia, P. K.: Retrieval of aerosol optical depth above clouds from OMI observations: Sensitivity analysis and case studies, J. Atmos. Sci., 69, 1037–1053, doi:10.1175/JAS-D-11-0130.1, 2012.

Vaughan, M. A., Powell, K. A., Kuehn, R. E., Young, S. A.,Winker, D. M., Hostetler, C. A., Hunt, W. H., Liu, Z., McGill, M. J., and Getzewich, B. J.: Fully Automated Detection of Cloud and Aerosol Layers in the CALIPSO Lidar Measurements, J. Atmos. Ocean. Tech., 26, 2034–2050, 2009.

Vernier, J. P., J. P. Pommereau, A. Garnier, J. Pelon, N. Larsen, J. Nielsen, T. Christensen, F. Cairo, L. W. Thomason, T. Leblanc, and I. S. McDermid: The tropical stratospheric aerosol layer from CALIPSO lidar observations, J. Geophys. Res., 114, D00H10, doi:10.1029/2009JD011946, 2009.

Wandinger, U., Tesche, M., Seifert, P., Ansmann, A., Müller, D., and Althausen, D.: Size matters: Influence of multiple scattering on CALIPSO light - extinction profiling in desert dust, Geophys. Res. Lett. , 37, L10801, doi:10.1029/2010GL042815, 2010.

Waquet, F., Cornet, C., Deuzé, J.-L., Dubovik, O., Ducos, F., Goloub, P., Herman, M., Lapyonok, T., Labonnote, L. C., Riedi, J., Tanré, D., Thieuleux, F., and Vanbauce, C.: Retrieval of aerosol microphysical and optical properties above liquid clouds from POLDER/PARASOL polarization measurements, Atmos. Meas. Tech., 6, 991-1016, doi:10.5194/amt-6-991-2013, 2013.

Waquet, F., Riedi, J., Labonnote, L. C., Goloub, P., Cairns, B., Deuzé, J. L., and Tanré, D.: Aerosol remote sensing over clouds using A-train observations, J. Atmos. Sci., 66, 2468–2480, doi:10.1175/2009JAS3026.1, 2009.

Washington, R. W., Todd, M. C., Middleton, N., and Goudie, A. S.: Dust-storm source areas determined by the total ozone monitoring spectrometer and surface observations, Ann. Assoc. Am. Geogr., 93, 297–313, 2003.

Winker, D. M., Tackett, J. L., Getzewich, B. J., Liu, Z., Vaughan, M. A., and Rogers, R. R.: The global 3-D distribution of tropospheric aerosols as characterized by CALIOP, Atmos. Chem. Phys., 13, 3345–3361, 2013.

Winker, D. M., Vaughan, M. A., Omar, A. H., Hu, Y., Powell, K. A., Liu, Z., Hunt, W. H., and Young, S. A.: Overview of the CALIPSO Mission and CALIOP Data Processing Algorithms, J. Atmos. Oceanic Technol., 26, 2310–2323, 2009.

Winker, D.: Accounting for multiple scattering in retrievals from space lidar, in: 12th International Workshop on Lidar Multiple Scattering Experiments, edited by: Werner, C., Oppel, U. G., and Rother, T., International Society for Optical Engineering, SPIE Proceedings, Vol. 5059, Oberpfaffenhofen, Germany, 128–139, 2003. International Society for Optical Engineering (SPIE Proceedings, Vol. 5059), 128–139, 2003.

Young, S. A., and Vaughan, M. A.: The retrieval of profiles of particulate extinction from Cloud Aerosol Lidar Infrared Pathfinder Satellite Observations (CALIPSO) data: Algorithm description, J. Atmos. Ocean. Tech., 26, 1105–1119, 2009.

Young, S. A., Vaughan, M. A., Kuehn, R. E., and Winker, D. M.: The retrieval of profiles of particulate extinction from Cloud-Aerosol Lidar Infrared Pathfinder Satellite Observations (CALIPSO) data: uncertainty and error sensitivity analyses, J. Atmos. Ocean. Tech., 30, 395–428, doi:10.1175/JTECH-D-12-00046.1, 2013.

Young, S. A.: Lidar analysis of lidar backscatter profiles in optically thin clouds. Appl. Opt., 34, 7019–7031, 1995.

Yu, H., and Zhang, Z.: New Directions: Emerging satellite observations of above-cloud aerosols and direct radiative forcing, Atmos. Environ., 72, 36-40, doi:10.1016/j.atmosenv.2013.02.17, 2013.

Yu, H., Chin, M., Winker, D. M., Omar, A. H., Liu, Z., Kittaka, C., and Diehl, T.: Global view of aerosol vertical distributions from CALIPSO lidar measurements and GOCART simulations: Regional and seasonal variations, J. Geophys. Res., 115, D00H30, doi:10.1029/2009JD013364, 2010.

Yu, H., Zhang, Y., Chin, M., Liu, Z., Omar, A., Remer, L.A., Yang, Y., Yuan, T., and Zhang, J.: An integrated analysis of aerosol above clouds from A-Train multi-sensor measurements, Remote Sensing of Environ., 121, 125-131, 2012.

Zhang, Z., and Platnick, S.: An assessment of differences between cloud effective particle radius retrievals for marine water clouds from three MODIS spectral bands, J. Geophys. Res., 116, D20215, doi:10.1029/2011JD016216, 2011.

Table 1 AOD retrievals for dust transport region over North Atlantic

Different Retrievals	**Mean AOD**	**AOD - AOD$_{OWC}$ (fractional difference)**
OWC constrained, AOD$_{OWC}$	0.247	
L2 standard, AOD$_{L2}$	0.183	-0.064 (-25.9%)
L2 rescaled, AOD$_{L2, rescaled}$	0.177	-0.070 (-28.3%)
Full column (S$_{a,model}$ = 40), AOD$_{FC,model}$	0.202	-0.045 (-18.2%)
Full column (S$_{a}$ = 45), AOD$_{FC,45}$	0.258	0.011 (4.5%)
CALIOP subtype	**Mean L2 AOD**	**L2 AOD Fraction**
Marine	0.000	0.0%
Dust	0.168	91.4%
Polluted dust	0.016	8.5%
Polluted continental	0.000	0.0%
Clean continental	0.000	0.1%
Smoke	0.000	0.2%

Table 2 Error budget estimates *

	Type $\frac{AOD_{L2} - AOD_{L2,res}}{AOD_{OWC} - AOD_{L2}}$	Detection $\frac{AOD_{L2,res} - AOD_{FC,model}}{AOD_{OWC} - AOD_{L2}}$	Lidar ratio $\frac{AOD_{FC,model} - AOD_{OWC}}{AOD_{OWC} - AOD_{L2}}$
Dust transport region	9.4%	-39.1%	-70.3%
Smoke transport region	-25.8%	-76.7%	2.5%

* Negative values indicate an underestimation and positive values represent an overestimation

Table 3 AOD retrievals for smoke transport region over South Atlantic

Different Retrievals	**Mean AOD**	**AOD - AOD$_{OWC}$ (fractional difference)**
OWC constrained, AOD$_{OWC}$	0.311	
L2 standard, AOD$_{L2}$	0.191	-0.120 (-38.6%)
L2 rescaled, AOD$_{L2, rescaled}$	0.222	-0.089 (-28.6%)
Full column (S$_{a,model}$ = 70), AOD$_{FC, model}$	0.314	0.003 (1.0%)

Full column (S_a = 75), $AOD_{FC,75}$	0.384	0.073 (23.5%)
CALIOP Subtype	**Mean L2 AOD**	**L2 AOD Fraction**
Marine	0.008	4.5%
Dust	0.001	0.2%
Polluted dust	0.016	8.4%
Polluted continental	0.007	3.9%
Clean continental	0.000	0.0%
Smoke	0.159	83.3%

Table 4 Mean AOD_{FC} using different S_a values

S_a (sr) S_a / $S_{a,model}$= 40	40 1.00	45 1.125	50 1.25	55 1.375	60 1.50
AOD_{FC} AOD_{FC} / AOD_{FC} ($S_{a,model}$= 40)	0.200 1.00	0.253 1.26	0.326 1.63	0.423 2.11	0.532 2.66

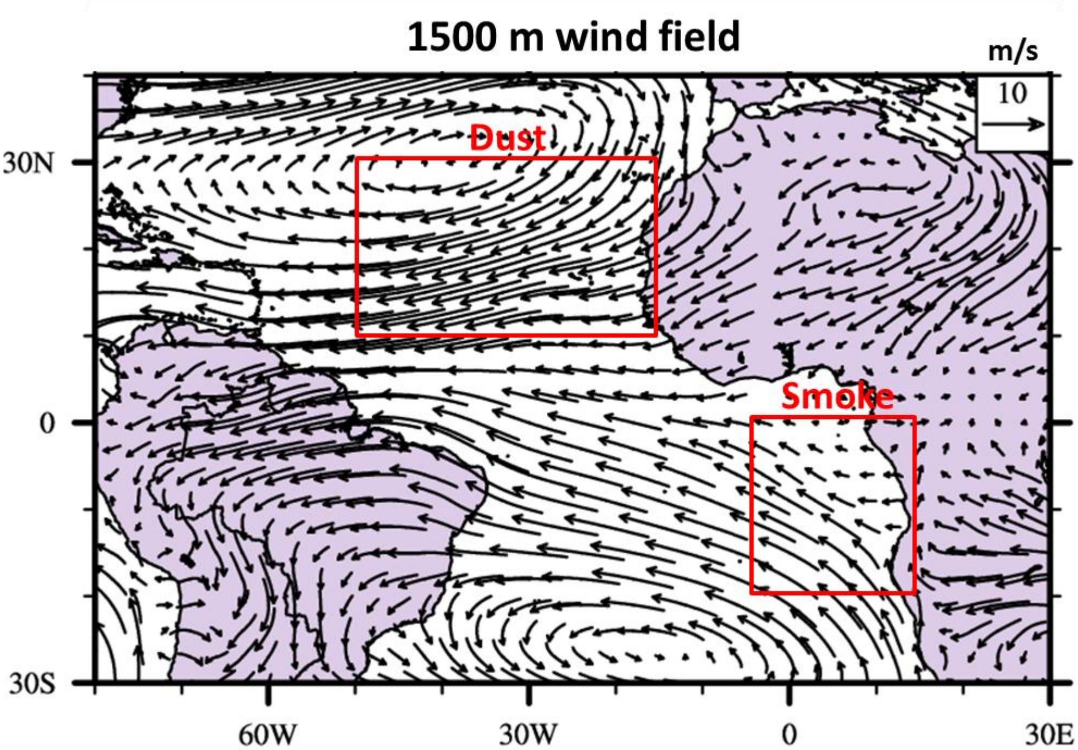

Figure 1. Spatial domains analyzed (red boxes) and wind fields (arrows) from ECMWF data for July and August from 2007 to 2012. The northern region (10°N-30°N, 50°W-15°W) is along the Saharan dust transport pathway over the tropical North Atlantic, while the southern region (20°S-0°, 5°W-15°E) is along the smoke transport pathway over the tropical South Atlantic.

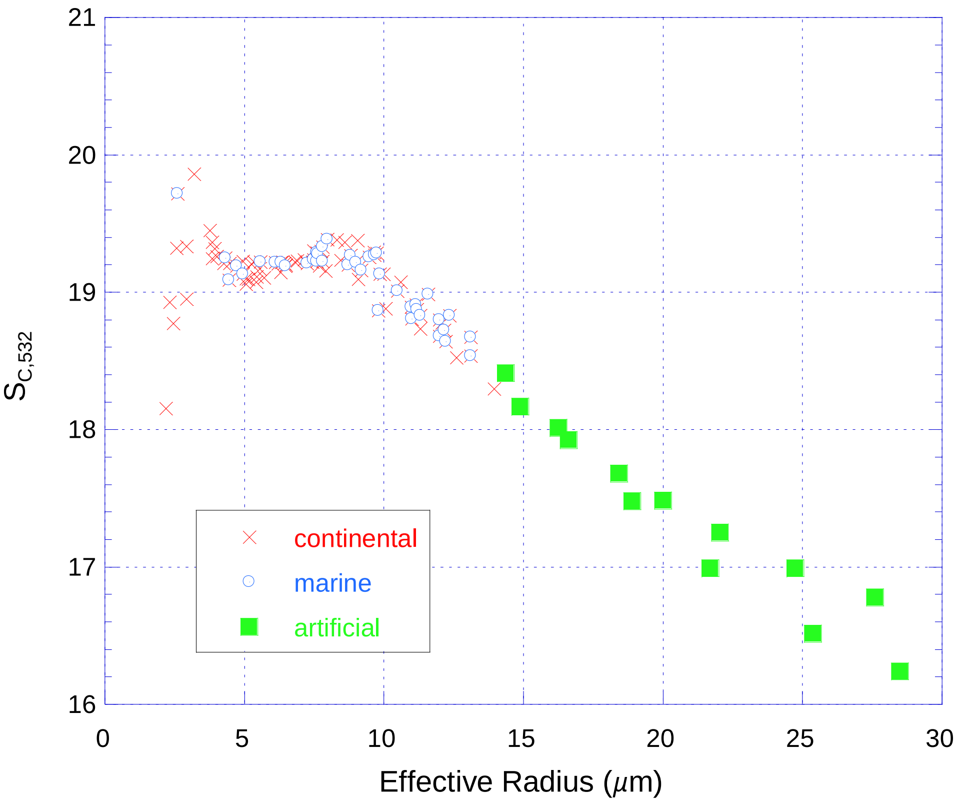

Figure 2. Water cloud lidar ratios calculated as function of effective droplet radius; red crosses and blue diamonds use in situ measurements of droplet radius (Miles et al., 2000), whereas green squares are derived from modeled distributions for clouds having larger droplet sizes.

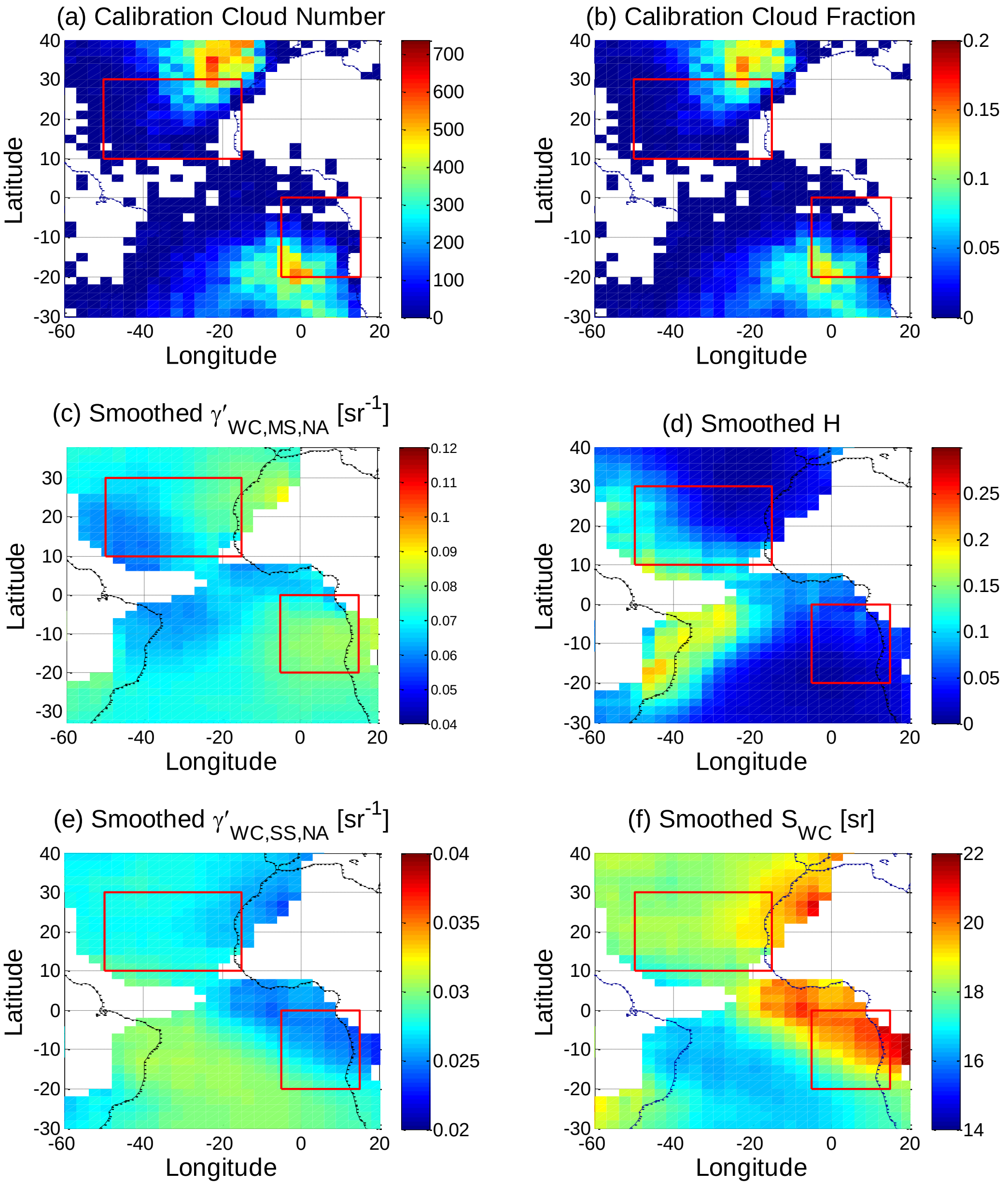

Figure 3. Spatial distributions of (a) number of calibration opaque water clouds above which no other cloud or aerosol layer was detected, (b) the fraction of calibration clouds relative to the total samples in each grid, (c) smoothed mean integrated attenuated backscatter, $\gamma'_{WC,MS,NA} = \int_{Cbase}^{Ctop} B'(r)dr$, from opaque water clouds in (a), (d) H calculated using Eq. (4), (e) mean integrated attenuated single-scattering backscatter, $\gamma'_{WC,SS,NA} = \gamma'_{WC,MS,NA}\mathrm{H}$, calculated from (c) and (d) and used as a reference in each grid box, and (f) water cloud lidar ratio $S_{WC} = 1/2\gamma'_{WC,SS,NA}$ (i.e., Eq.(5)) calculated from (e). The grid box size is 2°×3° (lat×lon). The smoothing window is a 5° x 5° grid. The white color represents the grids having no data samples. Data is from all nighttime CALIOP measurements during June – August in the years 2007 – 2012.

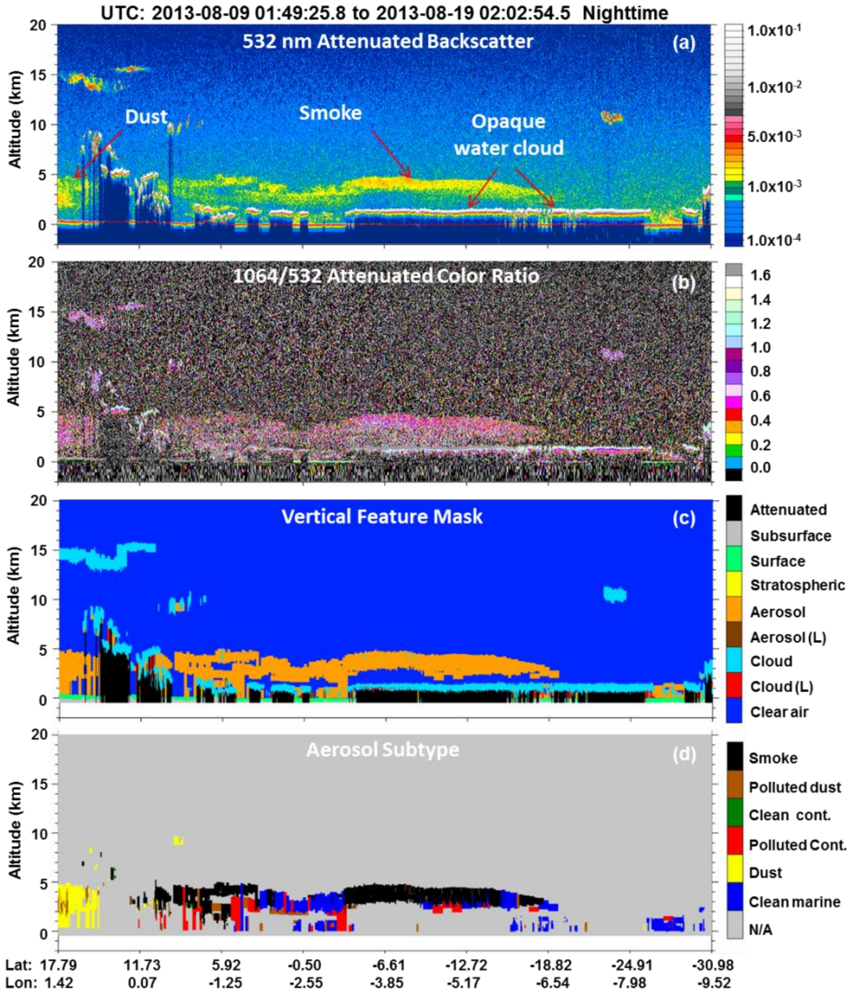

Figure 4. Example of CALIOP measurements of aerosols (smoke and dust) over water clouds made on August 9, 2013. (a) 532 nm attenuated backscatter, (b) attenuated backscatter color ratio (1064/532), (c) vertical feature mask, and (d) aerosol subtype.

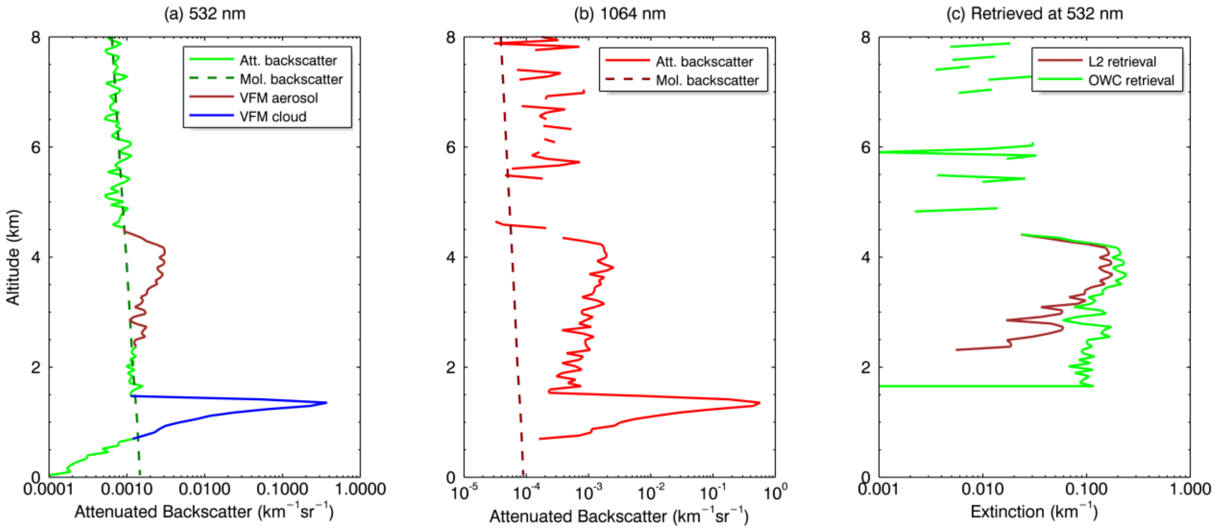

Figure 5. Solid curves in panel (a) and (b) show CALIOP attenuated backscatter profiles corrected for attenuation of molecular scattering and ozone absorption 532 nm (a) and 1064 nm (b). The dashed lines in these panels show the corresponding molecular backscatter profiles. Panel (c) shows the aerosol extinction profiles at 532 nm obtained from the standard L2 profile products (brown line) and retrieved in this paper using the OWC constrained technique (light green line). In both cases the retrievals were applied to a sequence of 5-km averaged L1 profiles, which in turn were averaged further for 4 consecutive 5-km profiles around 10°S, as shown in Figure 4. Brown and blue coloring in panel (a) indicate the data segments detected as aerosol and cloud in the standard L2 data processing.

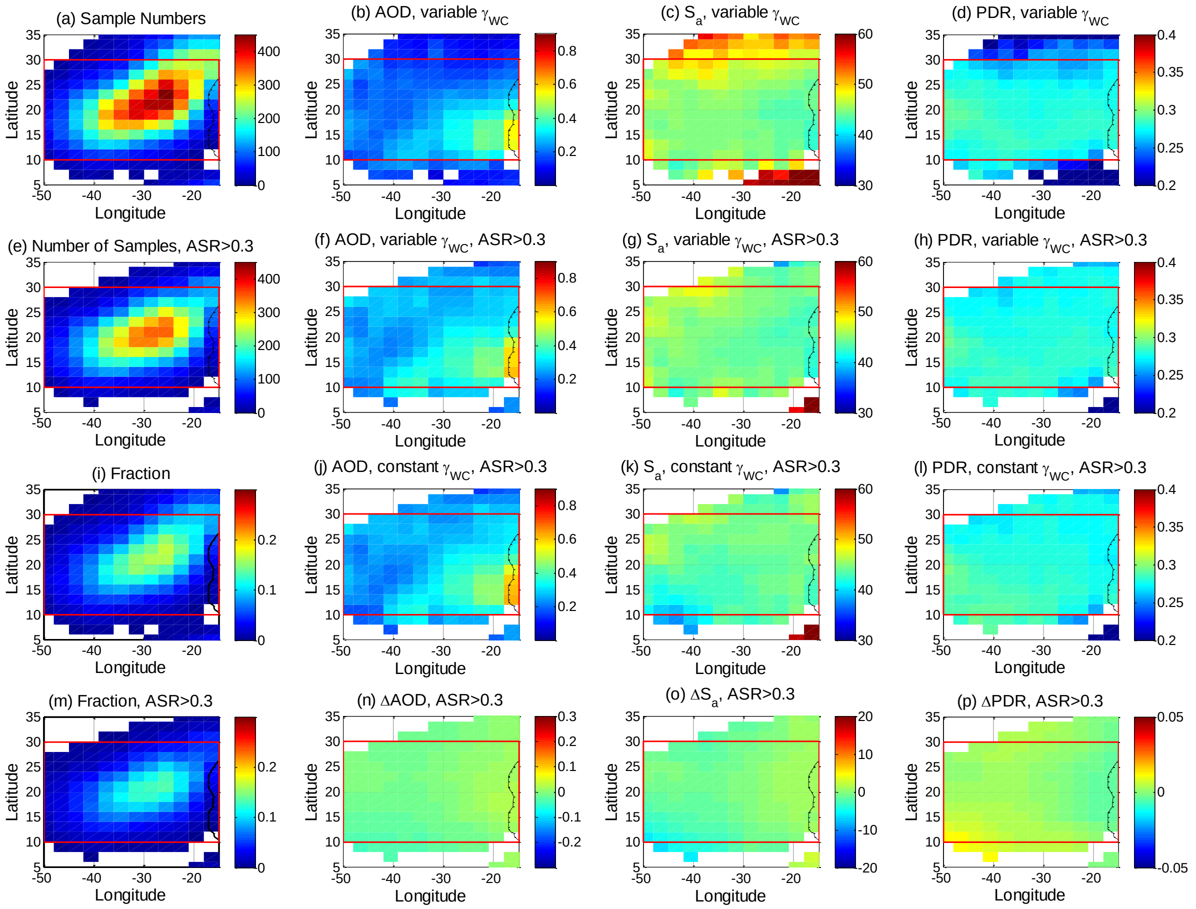

Figure 6. Analysis results in the dust region over the eastern North Atlantic from CALIOP data acquired during months of June – August in years of 2007 – 2012. (a) Number of samples, (b) AOD retrieved using the OWC technique with a location-dependent γ_{WC} for aerosol layers located above the opaque water clouds, and (c) S_a and (d) particulate depolarization ratio (PDR) retrieved using the OWC-retrieved AOD in (b) as a constraint. Shown in the second row of panels (e) – (h) are corresponding maps with data screening of ASR > 0.3 for the overlying aerosol layers (i.e., relatively weakly scattering aerosol layers are excluded). Panels (i) and (m) show the fraction of OWC retrievals relative to the total number of measurements in each grid, respectively, for all aerosol layers and moderately dense aerosol layers. The third row of panels (j) – (l) are corresponding maps using a constant $\gamma'_{WC,SS,NA}$ (0.0270 sr^{-1}) averaged over the spatial domain indicated by the red box. The bottom row of panels (n) – (p) are the difference of the corresponding quantities retrieved using a constant $\gamma'_{WC,SS,NA}$ and a location-dependent $\gamma'_{WC,SS,NA}$. The size of each grid box is 2°×3° (lat×lon). The spatial variability in the intrinsic dust optical properties S_a and PDR is seen to be larger for the retrievals that use a constant $\gamma'_{WC,SS,NA}$ (k and l) that for those that use a location-dependent $\gamma'_{WC,SS,NA}$ (g and h).

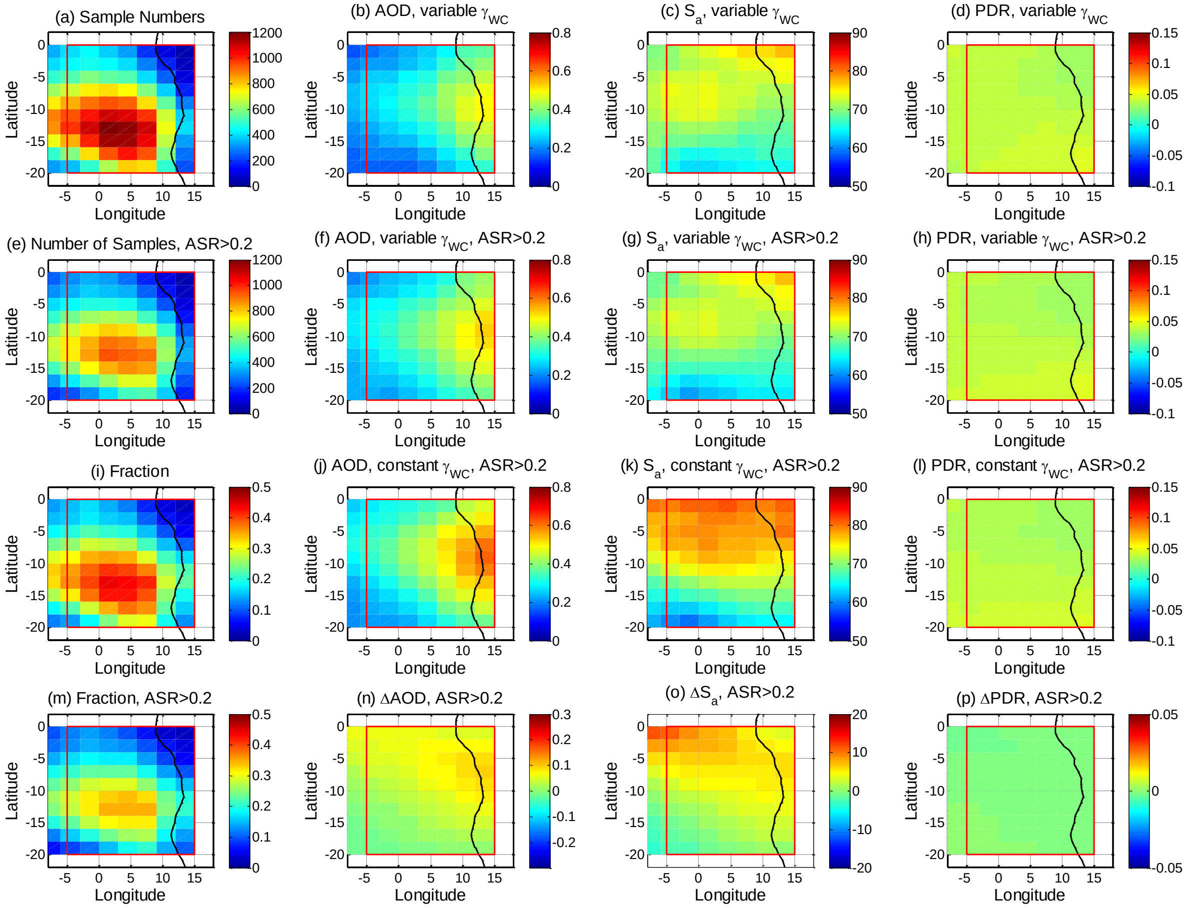

Figure 7. Analysis results in the smoke region over the eastern South Atlantic from CALIOP data acquired during months of July – September in years of 2007 – 2012. (a) Number of samples, (b) AOD retrieved using the OWC technique with a location-dependent γ_{WC} for aerosol layers located above the opaque water clouds, and (c) S_a and (d) particulate depolarization ratio (PDR) retrieved using the OWC-retrieved AOD in (b) as a constraint. Shown in the second row of panels (e) – (h) are corresponding maps with data screening of ASR > 0.2 for the overlying aerosol layers (i.e., relatively weakly scattering aerosol layers are excluded). Panels (i) and (m) show the fraction of OWC retrievals relative to the total number of measurements in each grid, respectively, for all aerosol layers and moderately dense aerosol layers. The third row of panels (j) – (l) are corresponding maps using a constant $\gamma'_{WC,SS,NA}$ (0.0260 sr^{-1}) averaged over the spatial domain indicated by the red box. The bottom row of panels (n) – (p) show the difference of the corresponding quantities retrieved using a constant $\gamma'_{WC,SS,NA}$ and a location-dependent $\gamma'_{WC,SS,NA}$. The size of each grid box is 2°×3° (lat×lon). A significant location-dependent trend is seen in the smoke S_a (j) retrieved using a constant $\gamma'_{WC,SS,NA}$.

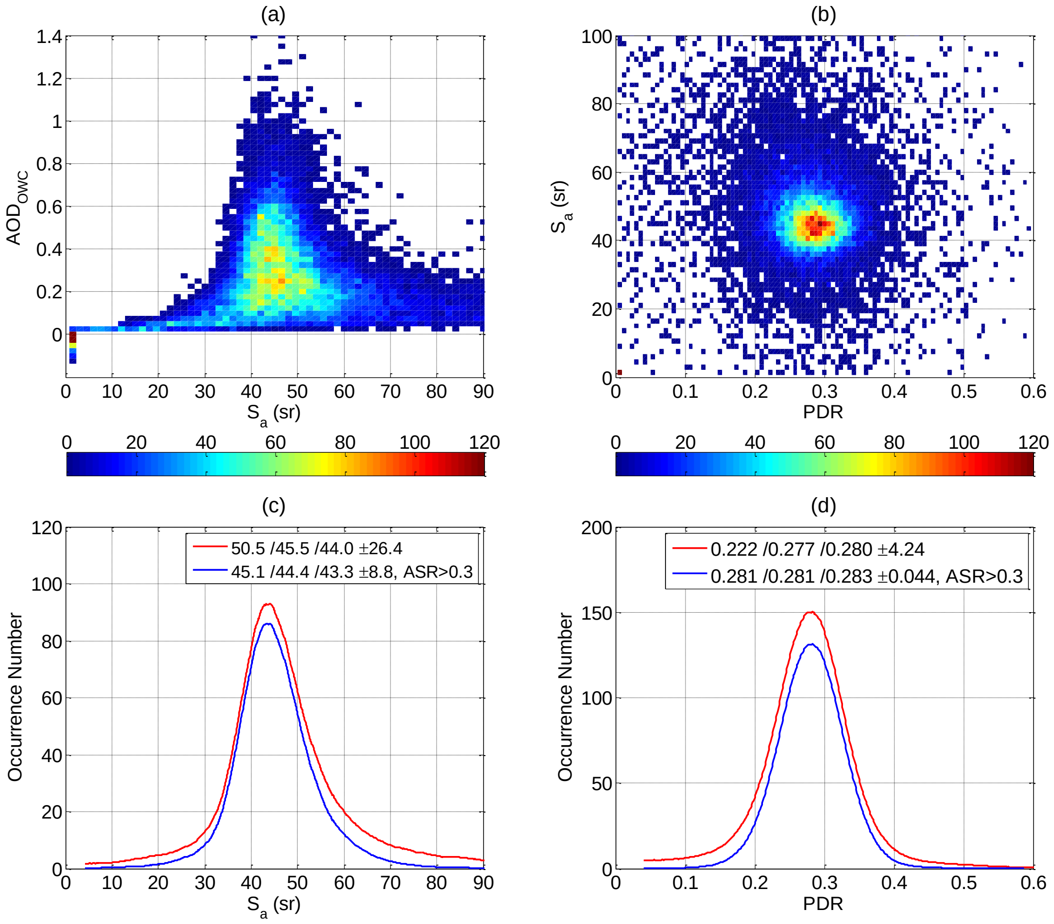

Figure 8. Analysis results for the dust transport region as indicated by the red box in Figure 6. The upper row shows 2-D distributions of (a) OWC AOD vs. S_a retrieved using OWC AOD as a constraint, (b) S_a vs. PDR, while the lower row shows histograms of (c) S_a and (d) PDR occurrence frequencies. The S_a distribution in (c) has a bin size of 0.1 sr and is smoothed, while the bin size for S_a in (a) and (b) is 1.5 sr. The PDR distribution in (c) has a bin size of 0.001 and is smoothed, while the bin size in (b) is 0.006. The red curves in (c) and (d) include all data and the blue curves are screened data using ASR>0.3. The numbers in the legends of are mean/median/mode ± standard deviation of S_a (c) and PDR (d).

(a) CALIOP OWC Retrieval

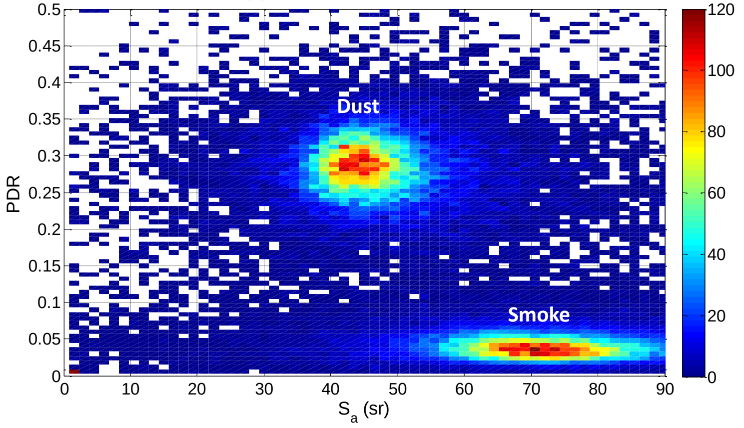

(b) HSRL Caribbean 2010

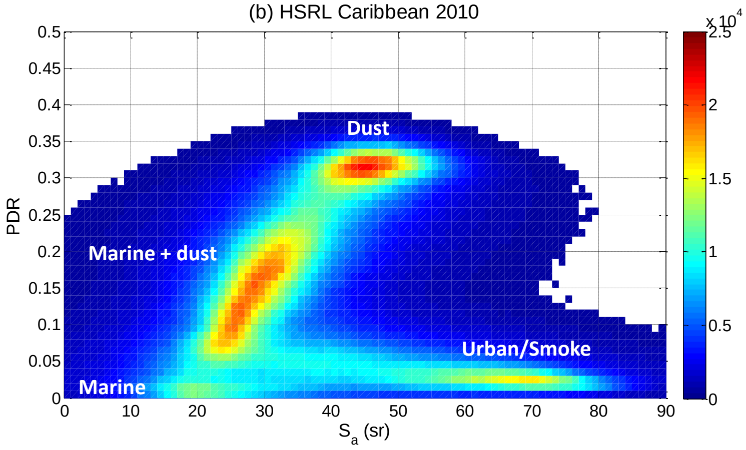

Figure 9. 2D distributions of lidar ratio and PDR (a) retrieved using the OWC contrained technique from six years of the CALIOP measurements and (b) measured by the NASA LaRC airborne HSRL during nine CALIOP validation fights during August 11-28, 2010 over the Caribbean Sea (see Burton et al., 2012 for more details about this validation campain). Panel (a) is a composite plot made from the OWC constrained retrievals from the dust transport region (i.e., Fig. 8b) and from the smoke transport region (i.e., Fig. 10b, with the sample number being scaled by a factor of 1/3). Note, each CALIOP sample was obtained for a layer extending from cloud top to 8 km, whereas each HSRL sample was measured for a 300 m range bin.

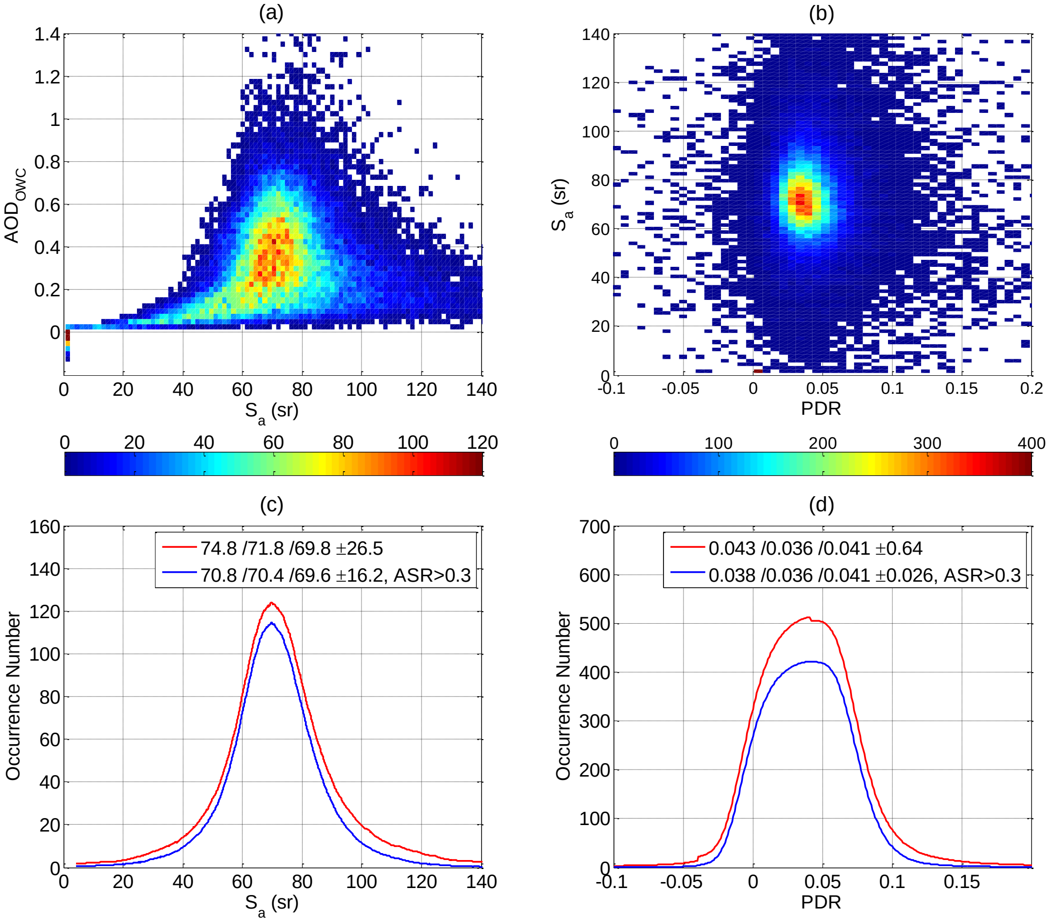

Figure 10. Analysis results for the smoke transport region as indicated by the red box in Figure 7. The upper row shows 2-D distributions of (a) AOD_{OWC} vs. S_a retrieved using AOD_{OWC} as a constraint and (b) S_a vs. PDR, while the lower row shows histograms of (c) S_a and (d) PDR occurrence frequencies. The S_a distribution in (c) has a bin size of 0.1 sr and is smoothed, while the bin size for S_a in (a) and (b) is 1.5 sr. The PDR distribution in (d) has a bin size of 0.001 and is smoothed, while the bin size in (b) is 0.006. The bin size for AOD in (a) is 0.025. The red curves in (c) and (d) include all data and the blue curves are screened data using ASR>0.2. The numbers in the legends of are mean/median/mode ± standard deviation of S_a (c) and PDR (d).

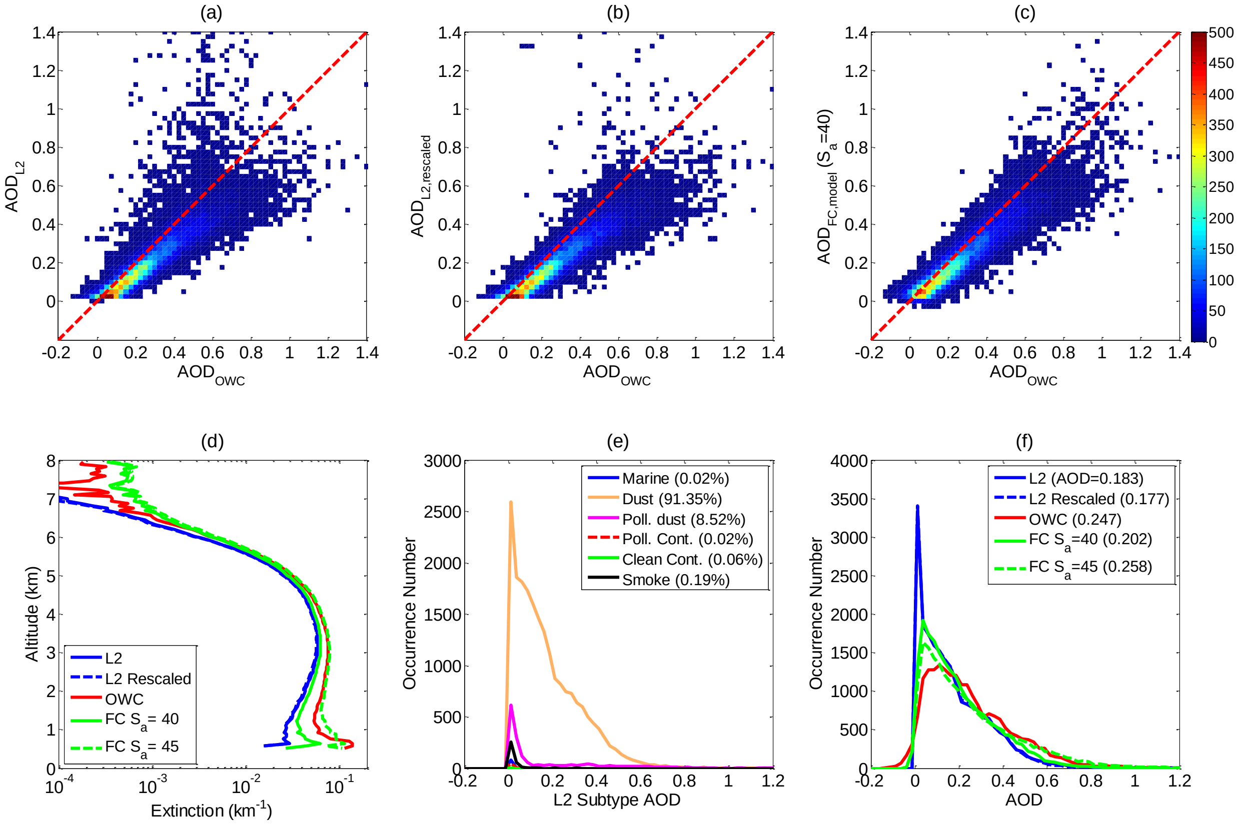

Figure 11. Analysis results for the dust transport region as indicated by the red box in Figure 6. The top row shows 2-D distributions of (a) AOD$_{L2}$ vs. AOD$_{OWC}$, (b) AOD$_{L2,res}$ vs. AOD$_{OWC}$, and (c) AOD$_{FC, mod}$ vs. AOD$_{OWC}$ for Sa = 40 sr. The bottom row shows (d) mean extinction profiles and histograms of occurrence number, (e) L2 AOD of different aerosol types, and (f) AOD retrieved using different retrieval methods. The bin size for AOD is 0.025.

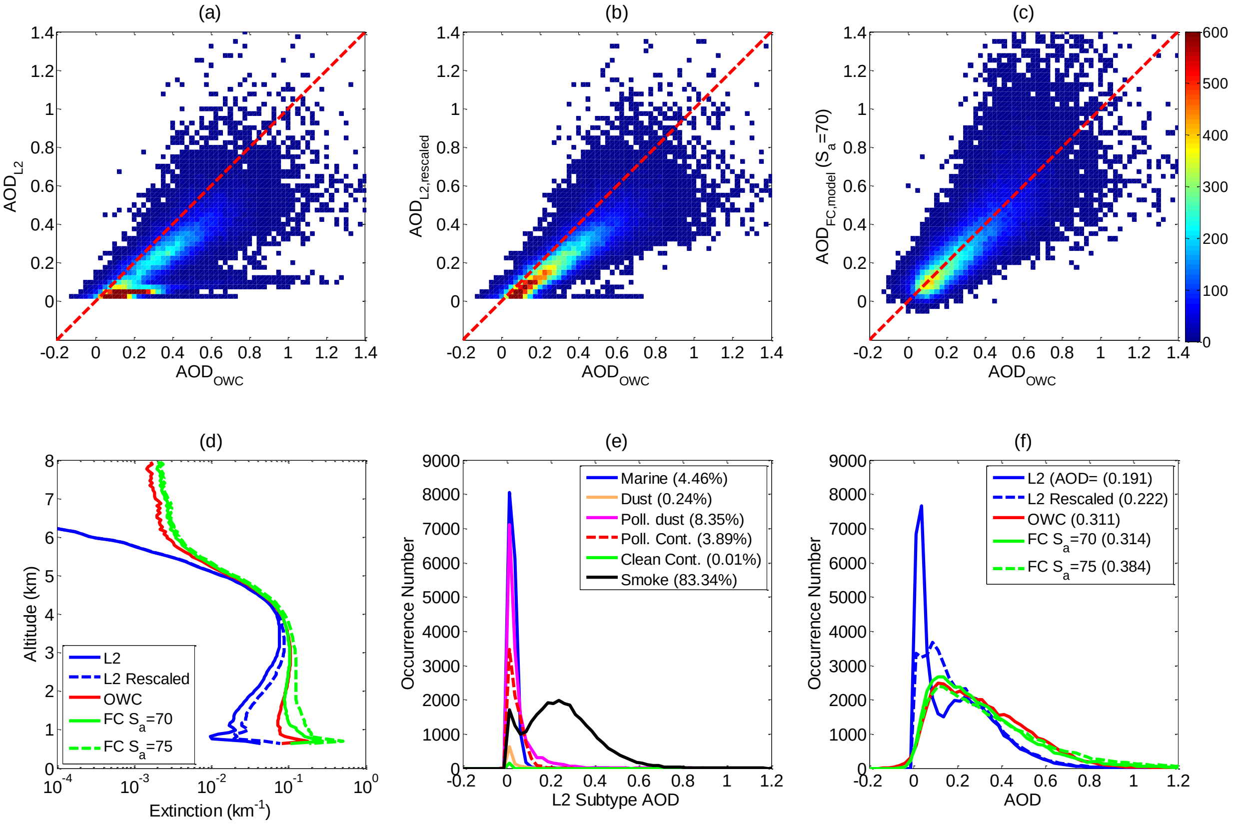

Figure 12. Analysis results for the smoke transport region as indicated by the red box in Figure 7. The top row shows two dimensional distributions of (a) AOD_{L2} vs. AOD_{OWC}, (b) $AOD_{L2,\ res}$ vs. AOD_{OWC}, and (c) $AOD_{FC,\ mod}$ vs. AOD_{OWC} for Sa = 70 sr. full column AOD using modeled dust $S_a = 40$ sr vs. AOD_{OWC}. The bottom row shows (d) extinction profiles and histograms of occurrence number, (e) L2 AOD of different aerosol types, and (f) AOD retrieved using different retrieval methods. The bin size for AOD is 0.025.

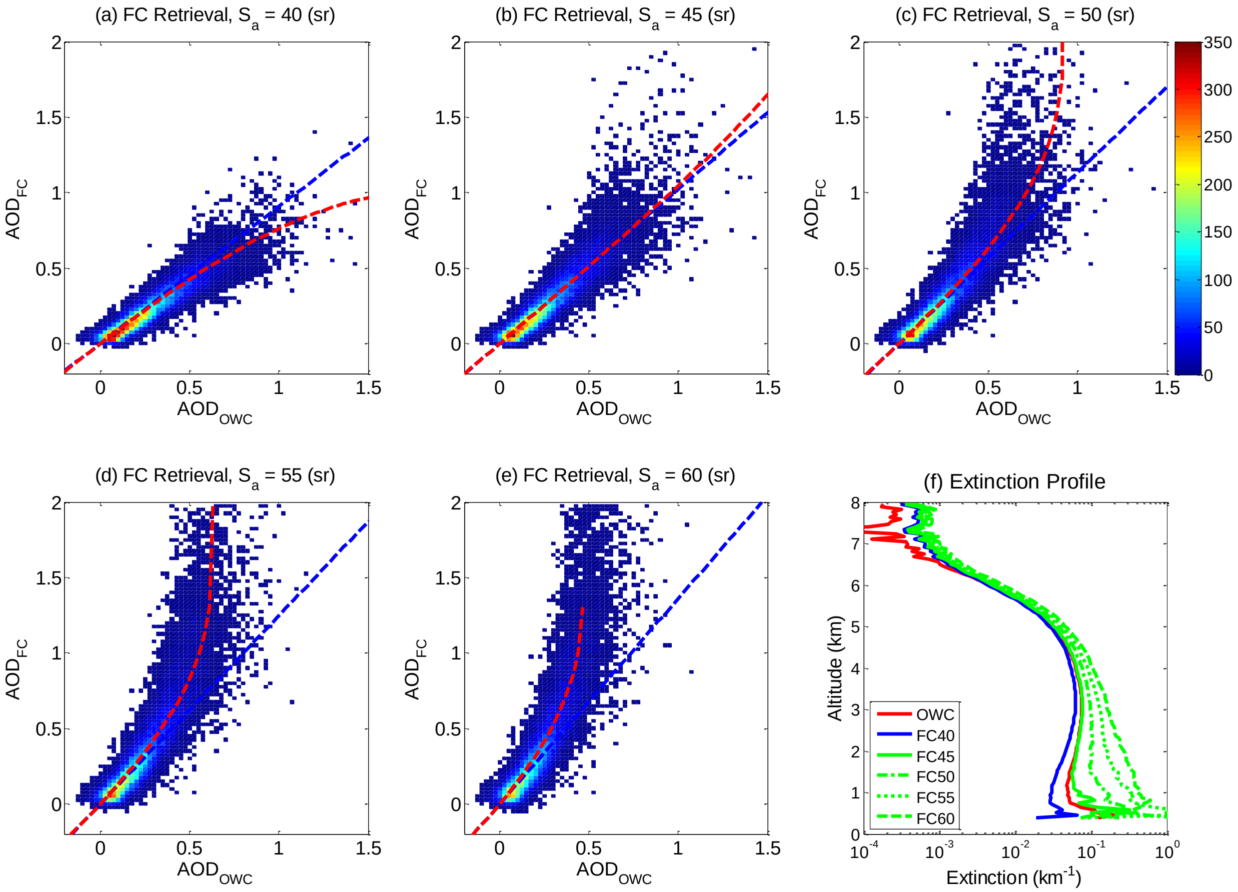

Figure 13. Distributions of FC AOD retrieved from the dust transport region using lidar ratios of (a) 40, (b) 45, (c) 50, (d) 55 and (e) 60 sr as a function of OWC AOD, and (f) corresponding extinction profiles. The blue line in panel (a) – (e) is a line having a slope of FC S_a/OWC S_a. The slope is (a) 40/44.4 = 0.91, (b) 45/44.4 = 1.01, (c) 50/44.4 = 1.13, (d) 55/44.4 = 1.24, and (e) 60/44.4 = 1.35. The red line is AOD estimated using Eq. (9) for a given lidar ratio used in the FC retrieval.

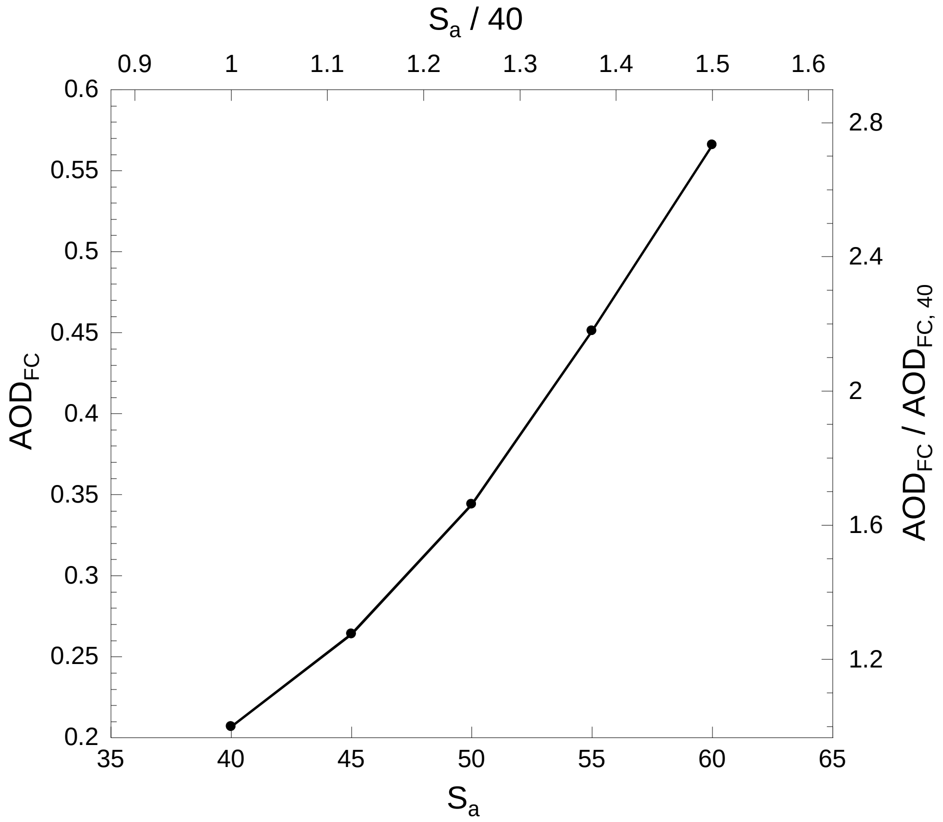

Figure 14. Mean AOD_{FC} as a function of S_a derived from the full column retrievals shown in Fig. 12.